Journal of Hydrology 626 (2023) 130305

Contents lists available at ScienceDirect

Journal of Hydrology

journal homepage: www.elsevier.com/locate/jhydrol

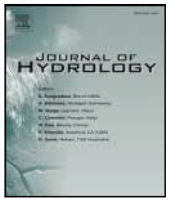

Research papers

Weekly mapping of surface water extent in the intertropical wetlands using spaceborne GNSS reflectometry

Pierre Zeiger [a,b,*], Frédéric Frappart [c], José Darrozes [d], Catherine Prigent [e,f], Carlos Jiménez [f,e], Luc Bourrel [d]

[a] Laboratoire d'Etudes en Géophysique et Océanographie Spatiale (LEGOS), UT3 Paul Sabatier, Toulouse, France
[b] CNRS, Institut des Géosciences de l'Environnement (IGE), Grenoble, France
[c] Interaction Sol Plante Atmosphère (ISPA), INRAE Bordeaux, Villenave-d'Ornon, France
[d] Géosciences Environnement Toulouse (GET), CNRS/IRD/CNES/UT3 Paul Sabatier, Toulouse, France
[e] CNRS, LERMA, Observatoire de Paris, Sorbonne Université, Université PSL, Paris, France
[f] Estellus, Paris, France

ARTICLE INFO

This manuscript was handled by Emmanouil Anagnostou, Editor-in-Chief, with the assistance of Yiwen Mei, Associate Editor.

Keywords:
GNSS-reflectometry
CYGNSS
Inundation dynamics
Surface water extent
Water fractions
Wetlands

ABSTRACT

As of today, the uncertain distribution and dynamics of inundations in the tropical wetlands cause large uncertainties in the quantification of the world's methane emissions. Long-term, global remote sensing observations currently rely on optical sensors, affected by cloud cover and vegetation, and on passive microwave imagery with a low spatial resolution. Global Navigation Satellite System Reflectometry (GNSS-R) L-band observations from space onboard the Cyclone GNSS (CYGNSS) mission can provide information about the dynamics of surface water at moderate to low spatial resolution and with a frequent revisit. In this article, we propose a methodology to compute the fraction of water contained in 0.1° pixels (~10 km) using CYGNSS reflectivity and Above Ground Biomass (AGB) maps. We produced a 1-year time series of water fractions with a weekly time sampling for the full coverage of CYGNSS between ±38° of latitude, from August 2018 to July 2019. We evaluated the results against regional reference maps of surface water based on MODIS, JERS-1, and PALSAR, and against the Global Inundation Extent from Multi-Satellite (GIEMS) dataset. CYGNSS water fractions represent well the spatial distribution and the seasonality of inundation extent for most of the tropical wetlands, with a global RMSD of 15.0 % against GIEMS. We found a likely overestimation when the soil moisture (SM) exceeds 0.3-0.4 cm^3/cm^3, *i.e.* for saturated soils where GNSS-R reflections are coherent, as the SM was not parameterized in our retrieval model. Despite this, the results are consistent in the entire intertropical band including over densely vegetated areas. These weekly water fractions for 2018-2019 with a 0.1° pixel size are distributed to contribute to further comparisons and hydrological researches.

1. Introduction

Wetlands strongly contribute to the hydrological and biogeochemical cycles while covering only 8% of the land surfaces (Davidson et al., 2018). They regulate river discharges to mitigate floods and supply water during the dry season (Bullock and Acreman, 2003; Acreman and Holden, 2013; Junk et al., 2013). They store an important carbon pool (Mitsch et al., 2013) and are the major natural source of methane emissions, up to 20%–30% (Whalen, 2005; Bergamaschi et al., 2007; Saunois et al., 2020). Yet, the spatial distribution of wetlands and the temporal variations of their extent largely contribute to uncertainties on methane emissions (Melton et al., 2013), particularly due to the lack of reliable estimations of surface water extent (Poulter et al., 2017).

The monitoring of surface water extent usually relies on remote sensing because of the sparsity of in-situ observations. Optical sensors are suited to detect open water but are particularly limited over vegetated wetland. High-resolution (30 m to 90 m) surface water datasets were derived from the 40-year Landsat archives (Verpoorter et al., 2014; Yamazaki et al., 2015; Feng et al., 2016; Pekel et al., 2016). For example, the Global Surface Water (GSW) dataset (Pekel et al., 2016) provides monthly estimates of permanent and seasonal water at 30 m spatial resolution since 1984. Other surface water datasets were derived at the regional scale using the Moderate Resolution Imaging Spectroradiometer (MODIS), especially over semi-arid regions such as the Inner Niger Delta (IND) and Lake Chad (Bergé-Nguyen and Crétaux, 2015; Pham-Duc et al., 2020), and also the Mackenzie Delta (Normandin

* Corresponding author at: Laboratoire d'Etudes en Géophysique et Océanographie Spatiale (LEGOS), UT3 Paul Sabatier, Toulouse, France.
E-mail address: pierre.zeiger@univ-grenoble-alpes.fr (P. Zeiger).

https://doi.org/10.1016/j.jhydrol.2023.130305
Received 10 May 2023; Received in revised form 25 August 2023; Accepted 24 September 2023
Available online 18 October 2023

et al., 2018). However, the visible and infrared signals are unable to penetrate neither cloud cover nor vegetation. As a consequence, the products based on Landsat and MODIS largely underestimate the wetland extent in tropical regions, especially the vegetated seasonal inundation.

Microwave signals are well suited for studying tropical wetland dynamics because they provide information day and night, penetrate cloud cover and partially the vegetation, especially at L-band due to the larger wavelength/lower frequency. Side-looking Synthetic Aperture Radars (SAR) can map surface water at high resolution (up to 1 m) as open water acts like a mirror and produces a low backscatter, and flooded vegetation produces a high backscatter due to the double-bounce effect (Richards et al., 1987). L-band SAR images were used to map inundations in the densely forested Amazon and Congo basins (Hess et al., 2003, 2015; Betbeder et al., 2014; Chapman et al., 2015; Rosenqvist et al., 2020). However, the use of SAR images was limited by a low temporal resolution before the launch of Sentinel-1, the low availability of L-band data, and the complexity to identify water signatures at large spatial scales with varying geophysical properties, incidence angles and different polarizations. This caused SAR data to be mainly used for near-real time flood monitoring at small spatial scales (Pulvirenti et al., 2011; Pierdicca et al., 2013; Westerhoff et al., 2013; Martinis et al., 2015; Twele et al., 2016), but not to derive a global surface water extent dataset. Recently, Martinis et al. (2022) proposed global inundation maps using the C-band SAR Sentinel-1 to complement optical data from Sentinel-2 in regions affected by cloud cover. However, this approach remains limited over forested regions. The monitoring of surface water extent changes in the tropics therefore relies on the use of passive microwave observations, as the brightness temperatures decreases in the presence of water, especially for the horizontal polarization (Choudhury, 1991; Sippel et al., 1994; Prigent et al., 2001; Parrens et al., 2017). Passive sensors are mostly limited by their coarse spatial resolution (25–50 km). They are used in multi-mission products like the Global Inundation Extent from Multi-Satellite (GIEMS, Prigent et al., 2007, 2020), which provides monthly surface water extent estimations at 25 km spatial resolution since 1992, based on the brightness temperatures from the Special Sensor Microwave Imager (SSM/I) and its successor, the Special Sensor Microwave Imager Sounder (SSMIS). This 25 km, monthly spatiotemporal resolution is insufficient to capture small water surfaces, flash flood or to study floodplain connectivity.

Global Navigation Satellite System (GNSS) Reflectometry (GNSS-R) can help in improving the representation of inundation dynamics, especially in tropical wetlands. This opportunistic remote sensing technique emerged the last decades with the rising number of GNSS satellites dedicated to positioning. It consists in measuring the GNSS L-band signals reflected by the Earth's surface, in a bistatic observational configuration where the transmitter and the receiver are separated (Martin-Neira et al., 1993; Zavorotny et al., 2014). The geophysical properties of the reflecting surface (or *glistening zone*) impact the signals, which are especially sensitive to the amount of surface water, the soil moisture, the surface roughness and topography, and the presence of vegetation. These fields of investigation recently benefited from the launch of spaceborne GNSS-R missions. The UK TechDemoSat −1 (TDS-1) was a first proof of concept that successfully allowed to retrieve either ocean wind speed and sea level (Foti et al., 2015; Clarizia et al., 2016), or land geophysical parameters like soil moisture and vegetation (Camps et al., 2016; Chew et al., 2016). It was followed by the NASA Cyclone GNSS (CYGNSS) mission, launched in 2016. It is a constellation of 8 Low Earth Orbit (LEO) micro-satellites carrying onboard a GNSS-R receiver (Ruf et al., 2016), and collecting observations in the intertropical band (±38° latitude). CYGNSS is dedicated to monitor the formation of tropical cyclones and supplies an ocean wind speed product (Clarizia and Ruf, 2016). Over land, it was used to retrieve soil moisture (Chew and Small, 2018; Al-Khaldi et al., 2019; Clarizia et al., 2019; Eroglu et al., 2019; Chew and Small, 2020a; Yan et al., 2020), and vegetation parameters such as the opacity (Pierdicca et al., 2021) or the Above Ground Biomass (AGB) (Carreno-Luengo et al., 2020). The combination of 8 receivers with four channels each allows a high sampling of the Earth's surface. Numerous studies exploited the frequent revisit of CYGNSS at low spatial resolution (sub-daily observations in pixels of ~25 km, Ruf et al., 2016).

The characteristics of CYGNSS make the mission a valuable tool for hydrological applications. Several studies exploited the observed sensitivity of CYGNSS reflectivity to the presence of surface water (Chew et al., 2018; Morris et al., 2019; Wan et al., 2019; Gerlein-Safdi and Ruf, 2019; Gerlein-Safdi et al., 2021; Ghasemigoudarzi et al., 2020; Rajabi et al., 2020; Zeiger et al., 2022; Chew et al., 2023). A high returned power is typically associated to a coherent scattering regime over smooth water or saturated soils (Chew and Small, 2020b; Loria et al., 2020). Early studies mapped floods following an extreme event (cyclone or typhoon), mostly using a threshold on CYGNSS reflectivity. The random walker segmentation method was also used to delineate flooded from non-flooded areas (Gerlein-Safdi and Ruf, 2019; Gerlein-Safdi et al., 2021). Jensen et al. (2018) also studied the relationship between floods, vegetation and CYGNSS reflectivity in a small subset of the Amazon basin. Over the same tropical wetland complex, Rodriguez-Alvarez et al. (2019) classified the open water, flooded vegetation and non-flooded land using CYGNSS reflectivity. All these studies were performed over small regions, as the detection of surface water at global scale is hampered by changes in the geophysical properties of the reflecting surface. Recently, Zeiger et al. (2022) demonstrated that CYGNSS reflectivity could be used to derive a surface water extent dataset in the entire intertropical area despite a large attenuation of the GNSS-R signals in dense forests. A clustering method based on Dynamic Time Warping (DTW) was applied to the time-series of reflectivity, and five clusters were defined depending on their inundation dynamics. This study dealt with the detection of surface water but did not compute the fractional inundation (or water fraction) in each 0.1° pixel. Chew et al. (2023) provided the first fractional inundation estimations based on CYGNSS, with a physical rather than statistical approach. The dielectric model employed requires the modeling of soil and water roughness that are highly variable and uncertain. Additional uncertainties are related to the spatial interpolation of sparse CYGNSS observations used to retrieve water fractions with a 3-km and 3-day spatiotemporal sampling, and to the attenuation of GNSS-R signals by the vegetation that was not parameterized in their dielectric model but only represented as a linear relationship between the reflectivity (in dB) and the AGB.

Because smooth water surfaces are associated to a coherent scattering regime, recent studies used the coherence of CYGNSS observations to map open water or flood extent. The coherence can be computed at high sampling rate (1 ms) using the phase from complex unprocessed signal samples, named *raw Intermediate Frequency* (IF) data (Li et al., 2021, 2022; Collett et al., 2022; Russo et al., 2022; Chapman et al., 2022). This characteristics permitted to detect water bodies with a width of ~100 m, including floods in densely vegetated areas, *i.e.* with an AGB of 250–300 Mg/ha (Li et al., 2021). However, although being very promising for surface water monitoring and for phase-delay altimetry (Cardellach et al., 2004; Li et al., 2017), this dataset is limited by the low amount of raw IF tracks recorded. Because the complex information is very large, it is incoherently averaged over 0.5 s (1 s before July, 2019) to produce the Level 1 Delay Doppler Maps (DDM) that represent the main CYGNSS data record. An operational flood monitoring based on raw IF data is not possible, at least before the launch of the future ESA's HydroGNSS mission planned for 2024 (Unwin et al., 2021). Hence, proxies for estimating the coherence based on the shape of Level 1 DDM were developed (Al-Khaldi et al., 2021a,b; Wang et al., 2022). Particularly, the DDM power-spread detector (DPSD) proposed in Al-Khaldi et al. (2021b) was further used to map permanent water in the full CYGNSS coverage at 1 km spatial resolution (Al-Khaldi et al.,

2021a). Seasonal floods can also be detected using this method but at lower spatial resolution.

Few studies took advantage of the high revisit of CYGNSS to map the inundation dynamics in the entire intertropical band. Furthermore, to the best of our knowledge, the contributions up to now considered a binary classification case to separate flooded and non-flooded areas, except a recently published article (Chew et al., 2023). In this study, the static classification of wet areas presented in Zeiger et al. (2022) and time-series of CYGNSS reflectivity are used to further derive weekly, 0.1° (~11 km at the equator) water fractions in the full CYGNSS coverage. Here, we build a statistical model using reference water fraction maps in an attempt to exploit the potential of CYGNSS for the monitoring of surface water extent spatiotemporal variations at both global and regional spatial scales. We particularly focus on producing realistic estimations over vegetated wetlands which cover a large fraction of the intertropical band and are poorly monitored up to now. The datasets used in this study are presented in Section 2, and Section 3 presents the water fraction retrieval methodology. The results and discussions of this work are given in Sections 4 and 5, respectively.

2. CYGNSS and reference datasets

2.1. CYGNSS Level 1 DDM

CYGNSS is mainly dedicated to ocean wind speed retrieval (Clarizia and Ruf, 2016) in order to monitor the formation of tropical cyclones (Ruf et al., 2016). The constellation's 8 Low Earth Orbit (LEO) micro-satellites cover the intertropical region (±38° latitude) with a high spatiotemporal revisit. Four GNSS reflected signals are simultaneously recorded by the Delay Doppler Mapping Instrument (DDMI) onboard each spacecraft, and incoherently averaged over 1 s (0.5 s, respectively) before (after) July 2019. The mean (median, respectively) revisit time over a 25 km ocean pixel was previously estimated to 7 (3) h in a 1-Hz sampling configuration (Ruf et al., 2016; Clarizia and Ruf, 2016).

A GNSS-R observation over the ocean has a low spatial resolution due to surface roughness (waves) that produces a diffuse scattering. The spatial resolution is much higher in the case of a dominantly coherent observation over smooth water surfaces or flat and saturated soils. In such configuration, it is approximately defined by the First Fresnel Zone (FFZ) that comprises most of the returned power (Camps, 2019). The FFZ size is ~0.6 km × 0.6 km for an observation near nadir, and increases with the incidence angle θ. Because the received power is incoherently averaged as CYGNSS spacecrafts move, the spatial resolution is degraded to 6.6 km along-track (with a 1 Hz sampling). However, CYGNSS Level 1 DDM can be used to detect water bodies down to few hundred meters according to both models (Loria et al., 2020) and observations (Al-Khaldi et al., 2021a). This is explained by the dominant contribution of the water fraction to the reflected power.

For the purpose of this study, we used the daily files from CYGNSS Level 1 Science Data Records, v3.0 (CYGNSS, 2020) distributed by the Physical Oceanography Distributed Active Archive Center (PODAAC). We used a 1-year dataset from August 2018 to July 2019 over the entire CYGNSS coverage. Only one year of data was used as in Zeiger et al. (2022) due to the high computational load required and for testing first the methodology. A further application to the ongoing 7-year CYGNSS records is likely. The study period corresponds to a 1 Hz sampling of the measurements (except for the last month), while twice more observations are performed monthly in the following years.

2.2. GIEMS surface water extent

We need external inundation datasets to compare with CYGNSS Water Fraction estimations. There are two global, long-term and low-resolution (0.25°) surface water extent products based on a combination of passive and active microwave observations: the Global Inundation Extent from Multi-Satellite v2 (GIEMS-2, Prigent et al., 2020) and the Surface Water Microwave Product Series (SWAMPS, Schroeder et al., 2015). We used GIEMS as numerous issues were pointed out in SWAMPS in an inter-comparison (Pham-Duc et al., 2017), although some were further corrected in the later releases (Jensen and Mcdonald, 2019). GIEMS surface water extent maps for 2018 and 2019 have been specifically processed for this study, averaged over 10 days. CYGNSS and GIEMS-2 water fractions are independent (see Section 3) and feed an inter-comparison of inundation extent and dynamics in both datasets (Section 4).

2.3. Regional maps of the flood dynamics

GIEMS spatial resolution is 0.25° (~28 km at the equator) which limits the detection of small water bodies. The sensitivity of CYGNSS to small river streams is therefore much higher (Zeiger et al., 2022). In this study, high resolution surface water extent maps were employed both in the retrieval methodology (see Section 3) and to compare with CYGNSS output water fractions. Global, high resolution datasets based on optical sensors like Landsat (Pekel et al., 2016) cannot detect flooded forests and so they are not suitable for comparison with CYGNSS in the intertropical band. We finally used a set of regional maps based on both optical and SAR data, which represent the diversity of the pan-tropical climate regions.

The first dataset consists in flood maps at 500 m spatial resolution based on MODIS surface reflectances from the MOD09A1 product (level 3/v6, 8-day binned). They are retrieved with the multi-threshold approach from Frappart et al. (2018) and Normandin et al. (2018) as a simplification of Sakamoto et al. (2007), using the Enhanced Vegetation Index (EVI, Huete et al., 1997) and the land surface water index (LSWI, Xiao et al., 2005) values. We computed MODIS flood maps for the 2018–2019 study period over three distinct climate regions: the Parana/La Plata river basin presenting flooded savannas and higher vegetation in the north, the Lower Mekong basin (LMB) with paddy fields and a strong seasonal flood signal around the Tonle Sap, and the Inner Niger Delta (IND) with low vegetation and bare soils.

Because MODIS is unable to detect flooded forests, especially in the Amazon and Congo basins, we need other high-resolution reference datasets covering dense tropical forests. This kind of dataset is rare and mostly based on L-band SAR images, which penetrate better the canopy layers. We used here the dual-season wetland classification in the Amazon basin from Hess et al. (1995, 2003). Based on JERS-1 L-band mosaics for the reference year 1995–1996, it provides a 100 m wetland mask at both low and high water stages (October–November 1995 and May–June 1996, respectively). Other similar datasets exist (see Fleischmann et al., 2022 for a comparison) but this one is still considered as a reference and has been widely used to compare with later studies.

Finally, flood maps at high and low water stages in the Cuvette Centrale of Congo were extracted from Betbeder et al. (2014). They are based on six images from the Phased-Array type L-band Synthetic Aperture Radar (PALSAR) onboard the Advanced Land Observing Satellite (ALOS) in 2009 and 2010, combined with Enhanced Vegetation Index (EVI) from MODIS and canopy height estimated with Light Detection and Ranging (LIDAR) data. Four wetland classes were initially delineated and correspond to open water, permanent inundations, long-term seasonal inundations, and short-term floods. Unlike MODIS and JERS-1 reference maps over the Parana, Niger, Mekong and Amazon basins, the PALSAR classification over the Cuvette Centrale of Congo was only used for validation and not in the retrieval methodology.

2.4. GlobBiomass AGB map

The detection of water using CYGNSS reflectivity is suitable for an AGB up to 200–300 Mg/ha according to a previous work (Zeiger et al., 2022). However, the attenuation of the GNSS-R coherent component for a high biomass content (Loria et al., 2020) is responsible for a decrease

in the reflectivity (Carreno-Luengo et al., 2020). In order to retrieve correct water fractions in flooded forests, we modeled the GNSS-R signal attenuation by the vegetation using the GlobBiomass AGB map at 3.2" spatial resolution (Santoro, 2018; Santoro et al., 2021). It is based on L-band ALOS/PALSAR and C-band ENVISAT/ASAR (Advanced Synthetic Aperture Radar) backscatters recorded in 2010. According to Santoro et al. (2021), GlobBiomass presents a bias over dense tropical forests where the dynamic range of the observations is low, but the spatial patterns are well reproduced.

Other biomass maps derived from EO observations including lidar such as the Global Ecosystem Dynamics Investigation (GEDI) (Dubayah et al., 2022) and the future SAR missions BIOMASS (Scipal et al., 2010) and NISAR (Kellogg et al., 2020) offer new opportunities to account for the attenuation of L-band signals in densely vegetated areas. As deforestation and subsequent regrowth can substantially modify CYGNSS reflectivity, the use of annual biomass updates could help in reducing surface water detection errors caused by land cover changes.

2.5. Other datasets

The AGB represents a static information and is related to the total woody volume, but the optical signals from MODIS can be affected by the vegetation growth. To evaluate the influence of the vegetation on the statistical comparisons performed, we used the Normalized Difference Vegetation Index (NDVI) maps from the MOD09A1 product (8-day binned level 3, version 6), derived from MODIS surface reflectance measurements. Moreover, our retrieval model neglects the influence of moisture variations to only consider the attenuation of GNSS-R signals by the vegetation (see Section 3). We nevertheless evaluated how the comparisons performed between CYGNSS, GIEMS, and MODIS Water Fractions vary according to the SM content. For this, we used the SMAP enhanced L3 9 km SM version 5 distributed by the National Snow and Ice Data Center (NSIDC) (O'Neill et al., 2021). The 9 km spatial resolution of SMAP enhanced L3 SM is close to the 0.1 °CYGNSS maps produced (see Section 3), and a global coverage on Earth is obtained every 3 days. All files from August 2018 to July 2019 were downloaded and further regridded to obtain reference SM values. Additionally, we filtered out deserts and open water areas as these targets were shown to produce false alarms and missed surface water detections, respectively (Al-Khaldi et al., 2021a; Zeiger et al., 2022). For this, we used the static open water and flood masks from the Regularly Flooded Wetland (RFW) dataset (Tootchi et al., 2019). Finally, the European Space Agency's (ESA) Climate Change Initiative (CCI) land cover maps were used for the input land cover information required (ESA, 2017).

2.6. Resampling of the datasets

The ancillary datasets were resampled to correspond to the spatiotemporal resolution of CYGNSS estimated water fractions (0.1° and 7 days). The average and standard deviation of AGB and NDVI per pixel were computed. We also upscaled the 500 m MODIS, 100 m JERS-1 and 100 m PALSAR flood maps at 0.1°. We computed the reference water fractions as a ratio between the number of flooded sub-pixels and the total number of sub-pixels in a given 0.1° pixel. Finally, we resampled SMAP SM maps from 9 km to 0.1° using a simple linear interpolation, and we computed the weekly averaged SM for all grid pixels.

The version of GIEMS we used is provided at ~25 km spatial resolution and 10-day temporal resolution. We performed the statistical comparison between CYGNSS and GIEMS at 7 days and 0.25° spatial resolution (see Section 4). Hence, we have upscaled CYGNSS water fractions at 0.25° spatial resolution for this comparison. GIEMS 10-day estimations were also upsampled to 7 days, using a weighted average of the two closest observations in time (with a maximum delta time of 7 days).

3. Methods

The CYGNSS dataset is first preprocessed as in Zeiger et al. (2022). The preprocessing steps include the extraction of each DDM peak power, the application of quality flags and of an ocean mask, and the removal of measurements when the peak power is located in the first or last three delay rows of the DDM, the latter being an indicator of topography effects that may degrade the measurement quality.

3.1. CYGNSS reflectivity computation

The GNSS-R signals are composed of an incoherent and a coherent components. The coherent part corresponds to specular reflections inside the FFZ, while the incoherent part corresponds to diffuse scattering all around. Bistatic scattering models (De Roo and Ulaby, 1994; Zavorotny and Voronovich, 2000; Voronovich and Zavorotny, 2018) have modeled both the coherent and the incoherent components. We computed CYGNSS surface reflectivity assuming a coherent reflection, which is in fact mostly associated to smooth inland surface waters (Chew and Small, 2020a; Loria et al., 2020). The reflectivity can be derived from the peak of a CYGNSS DDM (P_{DDM}), following De Roo and Ulaby (1994) and Gleason et al. (2020):

$$\Gamma(\theta_i) = \left(\frac{4\pi}{\lambda}\right)^2 \frac{P_{DDM}(R_r + R_t)^2}{G_r G_t P_t} \tag{1}$$

where λ is the wavelength ($\lambda_{GPS_L1} = 0.1903$ m), R_t and R_r are the *ranges* (distances from the specular point to the transmitter and the receiver, respectively), θ_i is the incidence angle, G_r is the receiver antenna gain, and $P_t G_t$ is the GPS Equivalent Isotropically Radiated Power (EIRP). In this study, the reflectivity is expressed in linear units and not in decibels. While the formulation in decibels was adopted in most of the literature (*e.g.* Chew and Small, 2020b; Chew et al., 2023), a linear scale is more convenient to formulate the linear relationships further used to invert water fractions (see Section 3.2). CYGNSS reflectivity was further normalized at a 0° incidence (nadir measurement) to correct the variations of the received power with the varying incidence angle, following Zeiger et al. (2022):

$$\Gamma = \Gamma(\theta_i = 0°) = \left(\frac{4\pi}{\lambda}\right)^2 \frac{P_{DDM}(R_r + R_t)^2}{G_r G_t P_t} \times \frac{1}{cos(\theta_i)} \tag{2}$$

We further aggregated the 1-year reflectivity dataset into a 7-day, 0.1° spatiotemporal grid. The resulting time series of reflectivity showed gaps because CYGNSS measurements are not evenly distributed over the Earth's surface. To reduce the number of data gaps, we applied to each pixel a 30-day moving window weighted with a Gaussian distribution (σ = 7 days). Then, we computed several statistical parameters describing the distribution of CYGNSS reflectivity in each pixel and per time step: the weighted average and standard deviation (Γ_{mean} and Γ_{std}, respectively), the median (Γ_{median}), and the nineteenth percentile ($\Gamma_{90\%}$). These parameters allowed the detection of flooded pixels in Zeiger et al. (2022) owing to a clustering method based on Dynamic Time Warping (Berndt and Clifford, 1994). In this study, they were further used to quantify the fraction of water contained in each pixel.

3.2. Inversion of the Water Fractions

Fig. 1 shows the complete flowchart for the retrieval of CYGNSS water fractions (WF). After the preprocessing and the gridding steps previously described, a linear model is established between the WF to be retrieved and Γ_{mean}. Only the methodology is described in this section whereas the results are presented in Section 4.1.

We used the clustering results from Zeiger et al. (2022) to select pixels likely to be affected by floods. We also filtered out desert pixels as defined by a flood occurrence of zero and a land cover composed of at least 90% of bare soils, using the RFW dataset from Tootchi

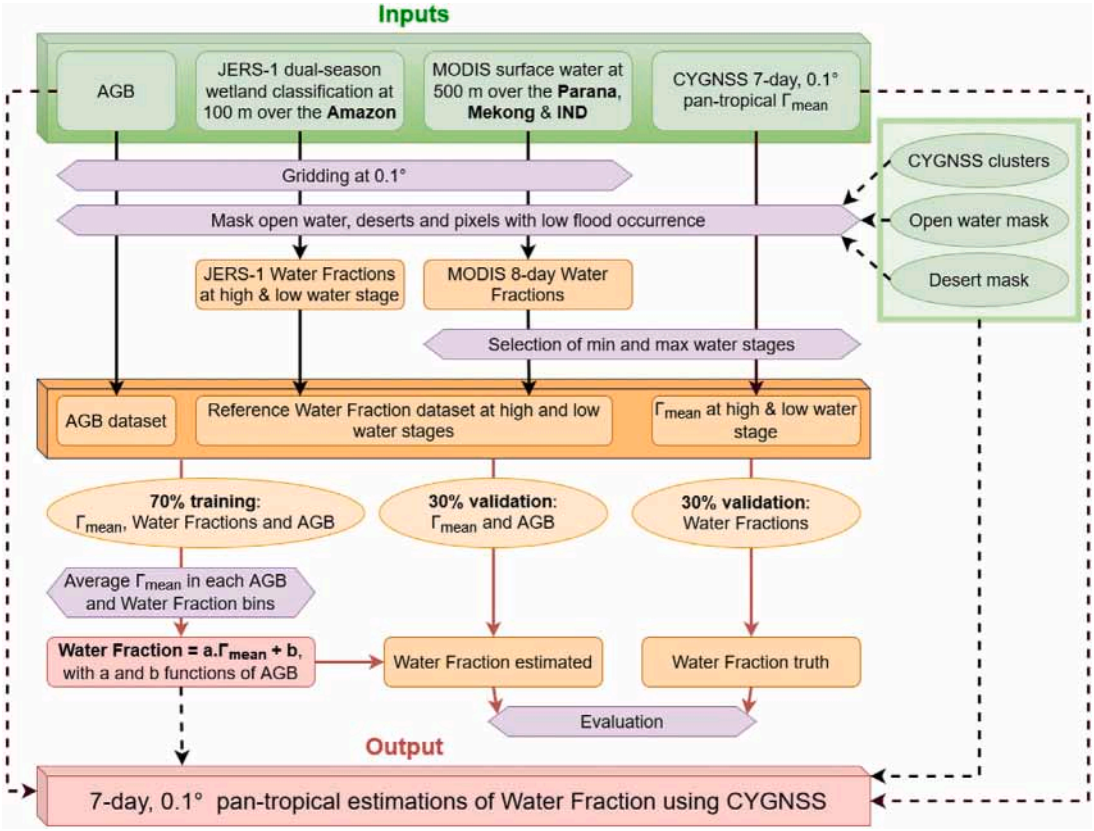

Fig. 1. Flowchart of the retrieval methodology for estimating CYGNSS Water Fractions at 0.1° spatial and 7 days temporal resolutions.

et al. (2019) and the ESA Climate Change Initiative (CCI) land cover maps (ESA, 2017). Fig. 2a shows the resulting desert mask which is mostly composed of the Sahara and the Arabian Peninsula. We also removed pixels containing more than 80% of open water (according to the RFW dataset). These masks are used to avoid false alarms over flat deserts that produce high reflectivity values (Al-Khaldi et al., 2021a; Zeiger et al., 2022), and misdetections of large open water bodies showing a quite low reflectivity due to the important roughness (*i.e.* waves) caused by wind (Chew and Small, 2020b; Loria et al., 2020), *e.g.* over the Lake Victoria and Tonle Sap (Zeiger et al., 2022).

The reference WFs used to train our linear model were extracted from the regional surface water extent products based on MODIS over the Parana, Mekong, and Niger basins (Normandin et al., 2018), and based on JERS-1 over the Amazon (Hess et al., 2003, 2015). The latter only provides wetland maps at high and low water stages in 1995–1996. Similar dual-season maps were therefore extracted from the 8-day MODIS product in order to ensure the consistency of the learning dataset (see Fig. 1).

The relationship between the reference WF and Γ_{mean} is dependant on the biomass content of the pixel, as shown in Section 4.1. The average GlobBiomass AGB of the pixel was therefore associated to each training and validation samples. Fig. 2b presents the distribution of the AGB for samples were the reference WF dataset is either derived from MODIS (in blue, 19 228 samples) or JERS-1 (in green, 11 878 samples, Amazon). The latter perfectly complements the lack of MODIS data for pixels with moderate to high biomass, *i.e.* for an AGB greater than 100–150 Mg/ha. Hence, the MODIS dataset contains 91.1% of the samples with an AGB lower than 50 Mg/ha, and only 0.6% of the samples with an AGB greater than 150 Mg/ha. The combination of both data sources makes the reference dataset consistent for an AGB range of 0 to ~280 Mg/ha. Fig. 2c–d present similar histograms for the reference WF and Γ_{mean} samples, with a predominance of low WF and low Γ_{mean} values.

The linear model was established as follows. First, we defined randomly a 70% training and a 30% validation datasets from the reference

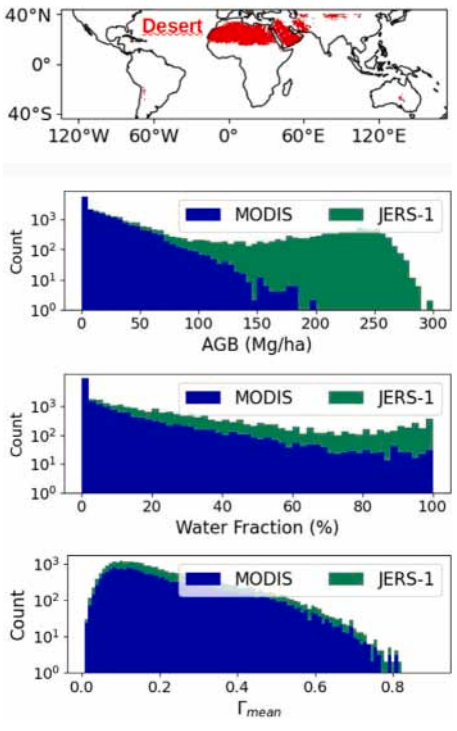

Fig. 2. Datasets used in the WF retrieval methodology. (a) Mask of non-flooded bare soils, (b) Distribution of the AGB for samples associated to MODIS (Parana, IND and LMB) or JERS-1 (Amazon) reference WF maps, (c–d) Similar histograms for the WF and Γ_{mean}, respectively. Bar widths are 5 Mg/ha and 2% for the AGB and WF histograms, respectively. (For interpretation of the references to color in this figure legend, the reader is referred to the web version of this article.)

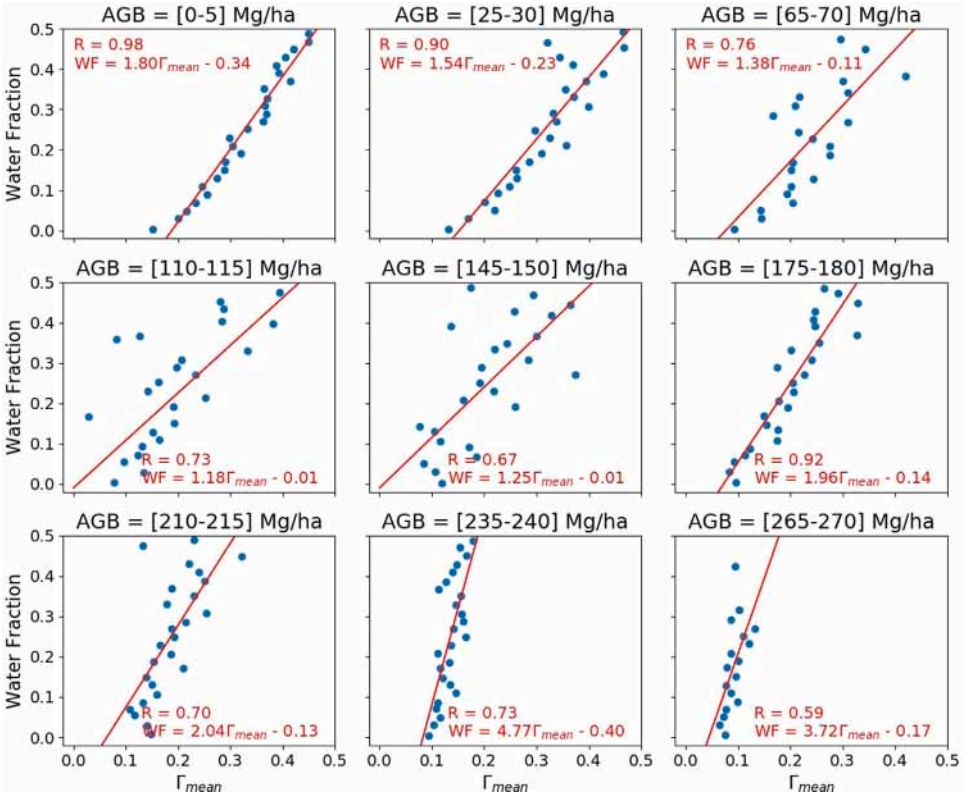

Fig. 3. Scatterplots of the average Γ_{mean} computed in 2% WF bins, for different AGB intervals ranging from [0–5] Mg/ha to [265–270] Mg/ha in the training dataset. The linear relationships between Γ_{mean} and the WF are shown in red for each interval, and the Pearson's correlation are also given. The slopes (a_{AGB}) and intercepts (b_{AGB}) of these linear fits are further parameterized as a function of the AGB (see Fig. 4). (For interpretation of the references to color in this figure legend, the reader is referred to the web version of this article.)

WF, the average AGB, and Γ_{mean} samples (see Fig. 1). We binned the training dataset along both the AGB (5 Mg/ha intervals) and the WF (2% WF intervals) dimensions and we computed the average Γ_{mean} in each bin. This permits to compute pairs of (WF, Γ_{mean}) equally sampled. It was implemented because the low-WF and low-Γ_{mean} values dominate the histograms of both variables (Fig. 2c–d), and as a consequence, the use of all samples resulted in biased high WF estimations. Our model looks for a linear relationship between the equally-sampled WF and Γ_{mean} in each AGB interval, where the attenuation by the vegetation is assumed to be constant. CYGNSS WF estimations (WF_{CYGNSS}) are computed as:

$$WF_{CYGNSS} = a_{AGB} \times \Gamma_{mean} + b_{AGB} \tag{3}$$

where a_{AGB} and b_{AGB} are the slope and the intercept and vary depending on the AGB. We tried to parameterize the relations between a_{AGB} or b_{AGB} and the AGB as first to fifth order polynomials. Based on the correlation and the Root Mean Square Error (RMSE) (see Section 4.1), a third order polynomial was selected as the optimal parameterization. We thus computed a_{AGB} and b_{AGB} as:

$$a_{AGB} = a_3 \times AGB^3 + a_2 \times AGB^2 + a_1 \times AGB + a_0 \tag{4}$$

$$b_{AGB} = b_3 \times AGB^3 + b_2 \times AGB^2 + b_1 \times AGB + b_0 \tag{5}$$

where a_i and $b_i, i \in [0,3]$ are the third order polynomial coefficients corresponding to the regression of a_{AGB} and b_{AGB} against the AGB, respectively. We computed the final robust coefficients as the average output of 100 random selections of the training dataset. The final equation for estimating WF_{CYGNSS} is:

$$\begin{aligned} WF_{CYGNSS} = {} & AGB^3 \left(a_3\Gamma_{mean} + b_3\right) + AGB^2 \left(a_2\Gamma_{mean} + b_2\right) \\ & + AGB \left(a_1\Gamma_{mean} + b_1\right) + a_0\Gamma_{mean} + b_0 \end{aligned} \tag{6}$$

Table 1
Coefficients of the third order polynomial fits of the slope and intercept against the AGB.

a_0	a_1	a_2	a_3	b_0	b_1	b_2	b_3
1.67	$-12.1\ e^{-3}$	$6.8e^{-5}$	0	−0.30	$5.6e^{-3}$	$-3.5e^{-5}$	$0.6e^{-7}$

4. Results

4.1. Linear relation between Γ_{mean} and the Water Fraction

In every AGB interval of the learning dataset, the average Γ_{mean} per 2% WF bin was computed. Fig. 3 presents some examples of the linear relationships found between these pairs of samples, for nine AGB intervals ranging from [0–5] Mg/ha to [265–270] Mg/ha. The Pearson's correlation between the Γ_{mean} and WF samples is also shown for each subplot. As it can be seen, it is generally high when removing the influence of the vegetation. Also, it is important to note that both the slope (a_{AGB}) and the intercept (b_{AGB}) of the linear relationships vary considerably with the AGB. Indeed, Fig. 4 presents the slopes (red circles) and intercepts (blue triangles) extracted in all the AGB intervals. The red and blue curves are the third order polynomial fits of a_{AGB} and b_{AGB} against the AGB, respectively. These curves fit well most of the samples with an AGB below 200 Mg/ha. The relationships obtained using only samples with an AGB below 200 Mg/ha are also shown with the dashed red and blue lines. The parameterization of the slope does not change but the parameterization of the intercept diverges for high AGB values. The full AGB range from 0 to 300 Mg/ha is required to obtain realistic estimations of the Water Fractions over densely vegetated regions, although values above 200 Mg/ha should be treated cautiously as they show a larger deviation.

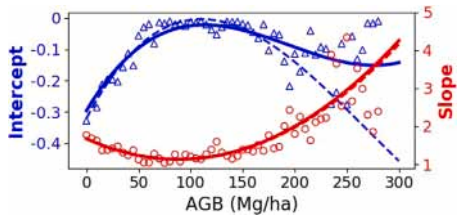

Fig. 4. Slopes (a_{AGB}, red circles) and intercepts (b_{AGB}, blue triangles) of the linear relationships between Γ_{mean} and the WF in each AGB interval. The red and blue curves are the third order polynomial fits of a_{AGB} and b_{AGB} against the AGB, respectively. The coefficients of this regression are listed in Table 1. The dashed red and blue lines indicate the same polynomial fits computed only with AGB samples lower than 200 Mg/ha. (For interpretation of the references to color in this figure legend, the reader is referred to the web version of this article.)

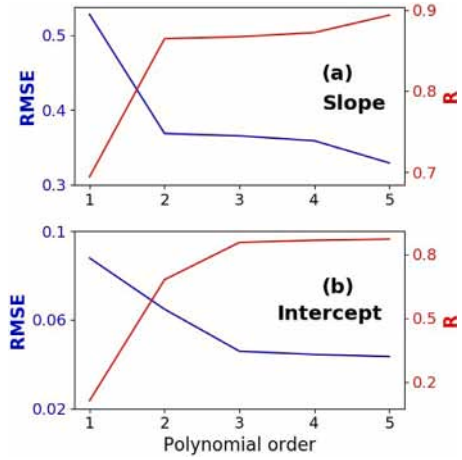

Fig. 5. Parameterization of the slope (a) and intercept (b) samples as a function of the AGB, using first to fifth order polynomials. For both cases the Pearson's correlation (R) and the RMSE are evaluated. The slope is correctly parameterized using a second order polynomial, while the intercept requires the introduction of a third order term following Eq. (6). (For interpretation of the references to color in this figure legend, the reader is referred to the web version of this article.)

The parameterization of the slopes and intercepts against the AGB were also tested using first to fifth order polynomial regressions. In every case, the Pearson's correlation and the Root Mean Square Error (RMSE) were computed between the slope/intercept samples and their fitted values. The results for both a_{AGB} and b_{AGB} are presented in Fig. 5. A second order polynomial sufficiently describes the relationship between the slope and the AGB. However, a third order term should be introduced to describe the relationship between the intercept and the AGB. The parameterization of these relationships in Eq. (6) therefore employs third order polynomials. The ultimate coefficients a_i and $b_i, i \in [0,3]$ are listed in Table 1 and correspond to the red and blue curves plotted in Fig. 4, respectively. Note that $a_3 = 0$ in accordance with the results shown in Fig. 5a.

Finally, bootstrapping was used to evaluate the robustness of the methodology across 100 iterations (results do not change significantly when increasing the number of iterations), with a random selection of the 70% training and 30% validation datasets. The coefficients a_i and $b_i, i \in [0,3]$ were determined at each iteration using the training dataset, and were used to compute predicted WF with the validation dataset. The RMSE and the Pearson's correlation were evaluated between the predicted and reference WF. Table 2 presents the results over 100 iterations for the entire validation dataset and for distinct 50 Mg/ha AGB intervals. The RMSE is around 0.20 (20%) over the entire AGB range. The best RMSE observed for an AGB greater than 250 Mg/ha could be a consequence of the lower average water fraction found under dense vegetation covers. A larger deviation between minimum and maximum results and lower correlations are indeed observed for the 250–300 Mg.ha AGB interval.

Table 2
RMSE and Pearson's correlation (R) between the reference Water Fractions and predictions from the validation dataset across 100 iterations, with a random selection of the training and validation samples. The mean, minimum, maximum and standard deviation values of RMSE are indicated with the mean R. Statistics are computed over the entire AGB range covered and over distinct 50 Mg/ha AGB intervals.

AGB range (Mg/ha)	$RMSE_{mean}$	$RMSE_{min}$	$RMSE_{max}$	$RMSE_{std}$	R_{mean}
All	0.207	0.202	0.212	$2.3e^{-3}$	0.606
0–50	0.199	0.191	0.207	$3.2e^{-3}$	0.551
50–100	0.235	0.219	0.250	$7.5e^{-3}$	0.641
100–150	0.235	0.218	0.249	$7.1e^{-3}$	0.567
150–200	0.212	0.197	0.230	$6.6e^{-3}$	0.538
200–250	0.204	0.194	0.215	$4.0e^{-3}$	0.506
250–300	0.187	0.166	0.208	$8.4e^{-3}$	0.437

4.2. CYGNSS pan-tropical Water Fractions

Weekly, 0.1° Water Fractions were estimated over the full coverage of CYGNSS (hereafter named WF_{CYGNSS}) using the coefficients listed in Table 1 and Eq. (6). This subsection briefly introduces the new product delivered here. Fig. 6 a shows the total number of weeks where inundations occur in each pixel during the 2018–2019 study period. Many areas show residual surface water throughout the year, as indicated by the number of weeks tending toward 52 in deep blue. Fig. 6b also shows the number of weeks with a Water Fraction greater than 20% in each pixel. The duration of inundations according to this metric largely decreases in most of the world. Large floodplains like the Orinoco and Llanos de Mojos wetlands in South America have a Water Fraction greater than 20% around 20 to 30 weeks a year. We show that only small WF values (<20%) are retrieved most of the time. These WF are particularly affected by the background noise and uncertainties related to the methodology proposed here (*e.g.* the Γ_{mean} vs. AGB model, soil moisture, etc.). However, they still present valuable information as a 20% WF represents around 20 km^2 of inundations.

Fig. 7 presents the time series of total surface water extent (SWE) in four latitude bins covering the entire study area. The [−38°, −20°] bin contains mostly inundations from the Parana basin with a maximum reached in May 2019. The [−20°, 0°] bin comprises large tropical wetlands, including the southern parts of the Amazon and Congo basins. It shows a large inundation peak during the spring with a maximum SWE around 500,000 km^2. The [0°, 20°] bin includes the northern parts of the Congo and the Amazon, the Orinoco basin, the Sahel and Southeast Asian basins like the Mekong. It shows a large inundation peak during the summer, more pronounced in 2018 with a SWE peaking at 500,000 km^2. Finally, the [20°, 38°] bin includes North American wetlands (below 38° latitude), the Ganges, Brahmaputra and Indus basins in the Indian subcontinent, and the Yangtze in China. It shows a maximum SWE during the summer reaching 400,000 km^2 in both August 2018 and July 2019. Overall, the phase difference between inundation patterns in the Southern and Northern hemispheres is well retrieved. All curves also show large amplitude variations except the [−38°, −20°] latitude bin dominated by the Parana floodplains.

4.3. Comparison of CYGNSS Water Fractions with GIEMS

Our WF_{CYGNSS} estimations were first compared to the fully independent estimations from GIEMS-2 (hereafter WF_{GIEMS}) over the entire coverage of CYGNSS (±38° latitude). The resampling of GIEMS-2 to a 7-day temporal resolution and the upscaling of CYGNSS to a 0.25° spatial resolution were described in Section 2.6. The global Root Mean Square Deviation (RMSD), bias and Pearson's correlation (R) were computed between WF_{CYGNSS} and WF_{GIEMS}. First, only the samples with non-null WF in both datasets were considered. We

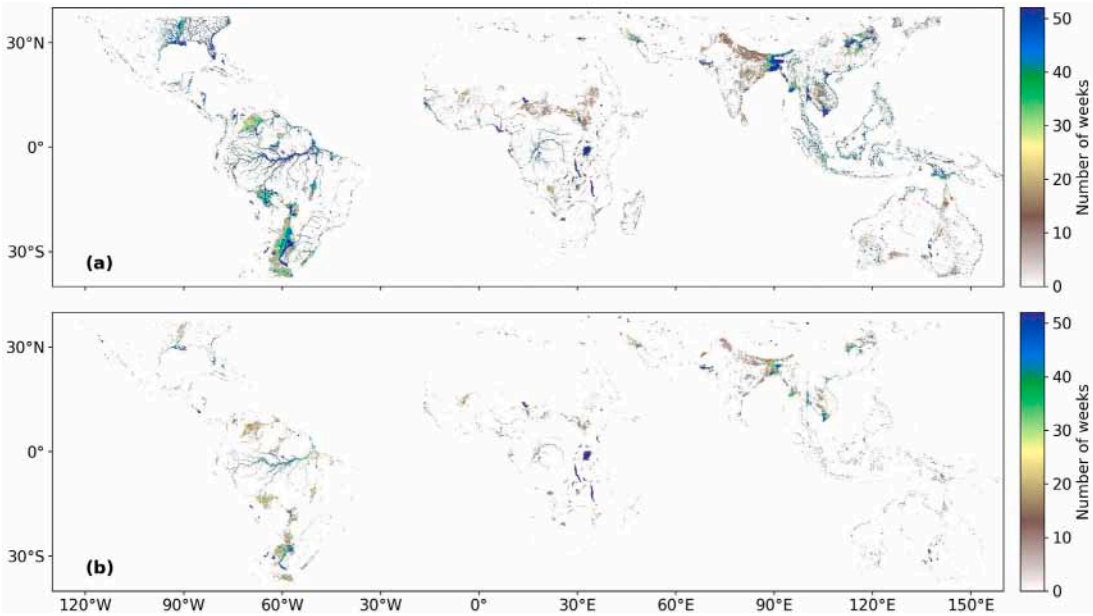

Fig. 6. Duration of inundations according to CYGNSS Water Fractions. (a) Number of weeks with a non-zero WF, and (b) Number of weeks with a WF greater than 20%. Open water areas based on the open water mask are filtered out in the retrieval and filled with a 100% WF. (For interpretation of the references to color in this figure legend, the reader is referred to the web version of this article.)

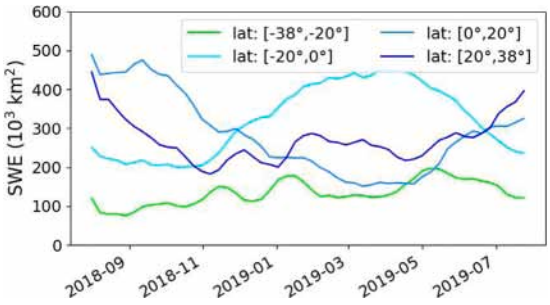

Fig. 7. Time series of cumulative CYGNSS surface water extent (SWE) grouped by latitude bins.

found a bias of −8.9% and a RMSD of 18.3% which falls to 15.9% when the bias is removed first (*i.e. unbiased* RMSD), with a correlation of 0.53 between both datasets. The global bias corresponds to lower WF_{CYGNSS} than WF_{GIEMS}, which is consistent with further results and especially Fig. 11. The coverage of non-null WF is also more restrictive in WF_{CYGNSS} (~8%) than in WF_{GIEMS} (~16%). When selecting all estimations with a non-null WF_{CYGNSS} only for the computation of the statistics (no condition over WF_{GIEMS}), we found a negligible bias (−0.6%) and a RMSD of 15.0%.

Fig. 8 presents the average WF_{CYGNSS} and WF_{GIEMS} in August 2018 (top two panels), during the wet season in most of the northern hemisphere, along with the bias and RMSD per pixel between the two datasets (bottom two panels). A positive bias (in red) means $WF_{CYGNSS} > WF_{GIEMS}$. Figure S1 also shows other monthly averaged WF_{CYGNSS} and WF_{GIEMS} in December 2018 and April 2019. Overall, both datasets are consistent and detect the major floodplains while CYGNSS shows a much higher sensitivity to small water bodies, especially around the Amazon and Congo tributaries. This is due to the higher native spatial resolution of CYGNSS coherent observations (~1 × 6 km). Conversely, WF_{GIEMS} is higher along the Amazon mainstream and in Southeast and East Asia. High soil moisture consecutive to monsoons likely drives this clear overestimation (see also Fig. 11). Finally, it is worth noting a positive bias along the coastlines, either due to contamination from the ocean which can affect both datasets, or to the presence of mangroves not detected by GIEMS mostly due to its lower spatial resolution. Global high-resolution mangrove maps like (Hamilton and Casey, 2016) could feed further work on this issue.

4.4. Regional comparisons

A better evaluation of the performances of WF_{CYGNSS} and WF_{GIEMS} is conducted at the scale of the river basin. In Fig. 9, both datasets are compared at low and high water stages with the inundation extent in the Amazon derived from JERS-1 (WF_{JERS}) in 1995-1996 (Hess et al., 2015). This comparison shows that most of the floodplains and river streams are delineated in WF_{CYGNSS} and the spatial correspondence with WF_{JERS} is good. The comparison between WF_{CYGNSS} and WF_{GIEMS} shows a seasonal flood signal with similar amplitude, and a better level of detail in WF_{CYGNSS} due to its higher spatial resolution. Finally, WF_{CYGNSS} and WF_{GIEMS} are generally lower than WF_{JERS}. This bias is particularly noticeable at high water stage, along the Amazon stream and in the Llanos de Mojos (~65°W and 15°S) in Bolivia.

Over the Cuvette Centrale of Congo, we used the wetland classification from Betbeder et al. (2014) to conduct a similar comparison which is shown in Figure S2. WF_{CYGNSS} matches well the water fractions extracted from the PALSAR classification at low water stage, but is much lower at high water stage (December) when the Cuvette Centrale of Congo is almost entirely flooded according to the reference maps. Both WF_{CYGNSS} and WF_{GIEMS} only detect water along the streams of the Congo River and its main tributaries, where the longest floods occur.

We also compared WF_{CYGNSS} and WF_{GIEMS} to MODIS WF estimations (WF_{MODIS}) in the IND, the LMB and the Parana basins. Figure S3 presents the annual maximum WF per pixel for all of the three datasets and the three study areas, with the associated surface water extent. The bias and RMSD per pixel were also computed and are shown in Fig. 10 between WF_{CYGNSS} and WF_{MODIS} (top two rows) and between WF_{CYGNSS} and WF_{GIEMS} (rows 3 and 4). Finally, the bottom row in Fig. 10 shows the annual maximum NDVI for further analysis.

WF_{CYGNSS} and WF_{MODIS} present similar spatial features in the IND and LMB. In these areas, a large spread is observed in WF_{GIEMS}

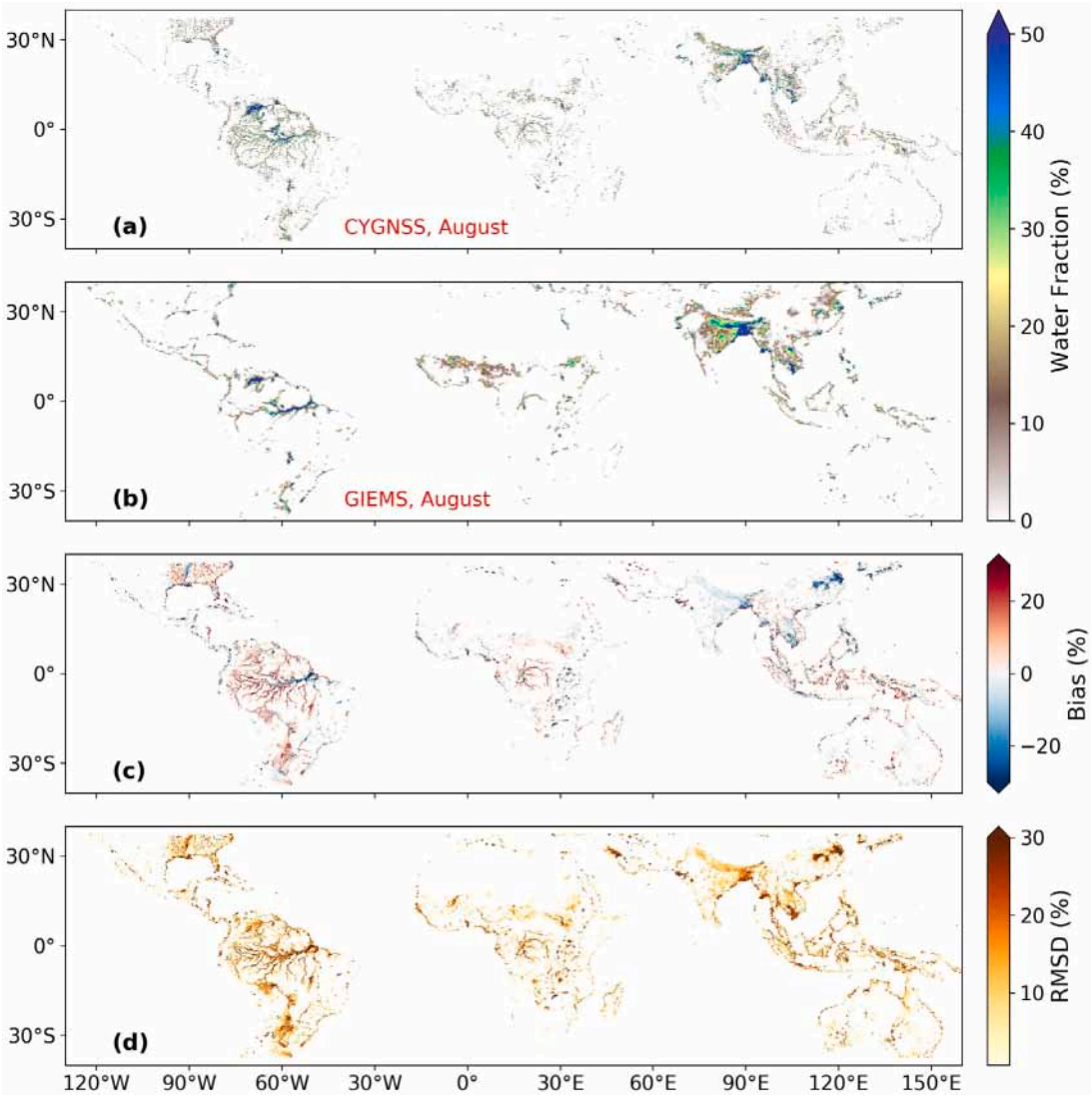

Fig. 8. Comparison of the Water Fractions estimated from CYGNSS and GIEMS, in percentage of a grid cell. (a) Average WF_{CYGNSS} and (b) average WF_{GIEMS} in August 2018. (c) Pixel-by-pixel bias between CYGNSS and GIEMS time series (red for $WF_{CYGNSS} > WF_{CYGNSS}$, blue otherwise), and (d) Pixel-by-pixel RMSD between WF_{CYGNSS} and WF_{GIEMS}. (For interpretation of the references to color in this figure legend, the reader is referred to the web version of this article.)

indicating a likely overestimation of flood extent during the wet season. We mostly observe a lower amplitude in WF_{MODIS} than in both WF_{CYGNSS} and WF_{GIEMS} (positive biases in Fig. 10a,f,k indicating $WF_{CYGNSS} > WF_{MODIS}$). It is interesting to notice that in the IND, we find opposed biases in the northern part ($WF_{GIEMS} < WF_{CYGNSS} < WF_{MODIS}$) where the maximum NDVI is very low (bare soils) and in the southern part ($WF_{GIEMS} > WF_{CYGNSS} > WF_{MODIS}$) where the maximum NDVI is in the range 0.4–0.6.

A much lower flood signal is observed in the Parana basin in WF_{MODIS}, as compared to WF_{CYGNSS} and WF_{GIEMS} which are close both in extent and amplitude. The annual maximum of NDVI shown in Fig. 10e,j,h clearly reveals that a higher NDVI is observed in the Parana (above 0.7–0.8) than in the IND and LMB. The presence of a denser vegetation characterized by higher NDVI values could explain this strong bias observed in the Parana between the optical-based WF_{MODIS} and other datasets based on microwave signals, which are less affected by the vegetation.

We computed the spatiotemporal RMSD, bias, and Pearson's correlation over the year in each basin between WF_{CYGNSS} and WF_{MODIS}, WF_{CYGNSS} and WF_{GIEMS}, and WF_{MODIS} and WF_{GIEMS}, and they are listed in Table 3. We previously filtered out all the samples having a WF equals to zero in either one of the two datasets used in the comparison. A positive bias is found between WF_{CYGNSS} and WF_{MODIS}, especially in the Parana basin (17.3%). The RMSD ranges from 18.3% (Mekong) to 26.2% (Parana), while the correlation ranges from 0.42 (Parana) to 0.69 (Mekong). The comparison between WF_{CYGNSS} and WF_{GIEMS} shows a smaller bias, with a RMSD ranging from 19.1% (Mekong) to 24.9% (IND) and a correlation around 0.60. Finally, the comparison between WF_{GIEMS} and WF_{MODIS} shows a strong positive bias up to 23.3% in the IND. The RMSD ranges from 17.4% (Mekong) to 31.8% (IND), and the correlation ranges from 0.50 (Parana) to 0.65 (Mekong). Overall, the large deviation between the three datasets is illustrated by a RMSD of ~20% and correlations of ~0.60. Interestingly, MODIS does not have the closest comparison to CYGNSS despite being used in the methodology. Both WF_{CYGNSS} and WF_{GIEMS} show a positive bias when compared to WF_{MODIS}, which could be due either to an overestimation of WF_{CYGNSS} and WF_{GIEMS} with soil moisture, or to an underestimation of WF_{MODIS} because of the high vegetation cover during the wet season.

Finally, for the samples with $WF_{CYGNSS} = 0$, the mean (median) values of WF_{GIEMS} and WF_{MODIS} are 1.9% (0%) and 0.9% (0%), respectively, and the RMSD is 6.5% for WF_{GIEMS} and 4.0%

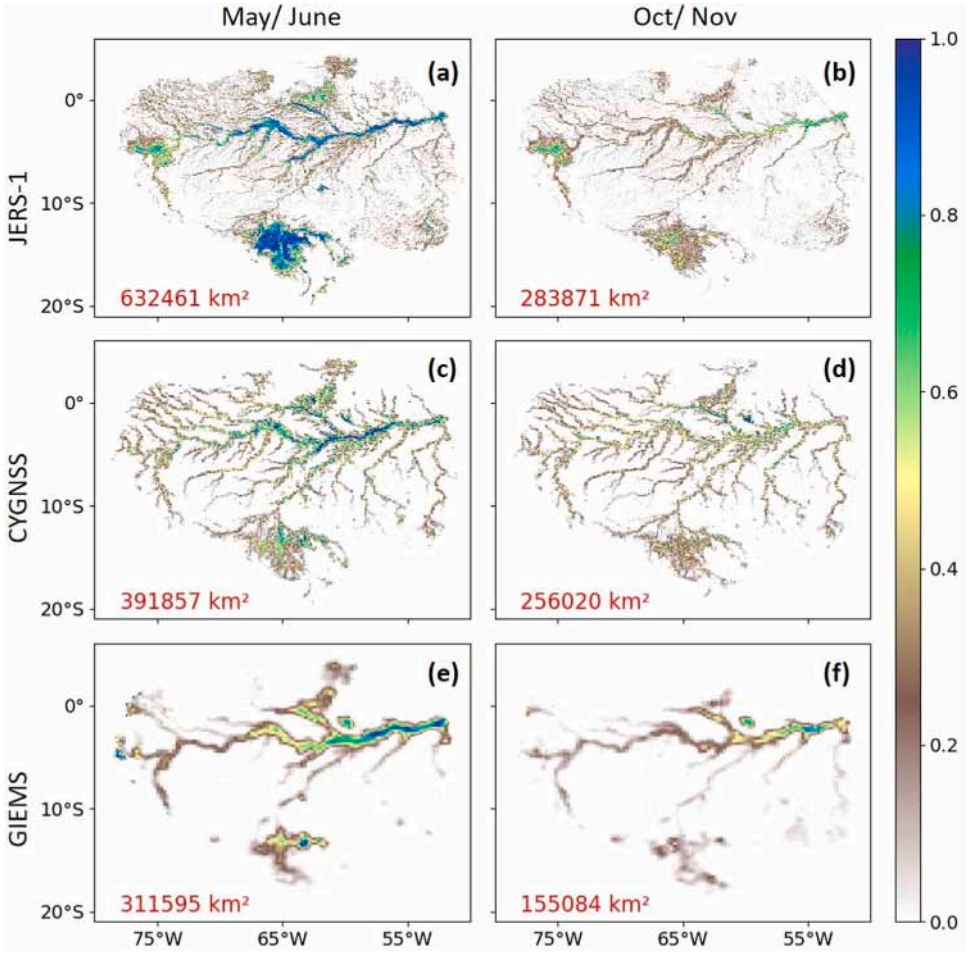

Fig. 9. Maximum Water Fraction at high water stage (May/June) and low water stage (October/November) in the Amazon basin, from JERS-1 (in 1995–1996), CYGNSS and GIEMS (both in 2018–2019). (a) JERS-1 high water, (b) JERS-1 low water, (c) CYGNSS high water, (d) CYGNSS low water, (e) GIEMS high water, and (f) GIEMS low water. For each case, the corresponding total surface water area is shown in red. (For interpretation of the references to color in this figure legend, the reader is referred to the web version of this article.)

Table 3
Statistics of the regional comparison between CYGNSS and MODIS **(C-M)**, CYGNSS and GIEMS **(C-G)** MODIS and GIEMS **(M-G)** Water Fractions, using all the estimations from August 2018 to July 2019. The columns present the RMSD, bias, and correlation (R) over the Inner Niger Delta (IND), the Mekong basin and the Parana basin. The samples with no water at all in either one of the two datasets compared are excluded from the computation.

	$RMSD_{IND}$	$Bias_{IND}$	R_{IND}	$RMSD_{MEK}$	$Bias_{MEK}$	R_{MEK}	$RMSD_{PAR}$	$Bias_{PAR}$	R_{PAR}
C-M	21.7%	8.9%	0.56	18.3%	10.5%	0.69	26.2%	17.3%	0.42
C-G	24.9%	−7.5%	0.61	19.1%	−1.7%	0.61	20.4%	8.3%	0.59
G-M	31.8%	23.3%	0.59	17.4%	9.8%	0.65	18.7%	7.8%	0.50

for WF_{MODIS}. These values statistically illustrate the low number of missed detections in this comparison.

4.5. Inundation extent dynamics

The surface water extent in each pixel can be easily computed by multiplying the WF by the pixel's size (~90–110 km^2). This step permits to analyze time series of surface water extent, either at the pixel's scale or aggregated over a particular area like a given river basin. Fig. 11 presents the results of this analysis conducted at the scale of the river basin, for study areas located in South America (the Orinoco, Amazon and La Plata/Parana), in Africa (the IND, Lake Chad and Congo), and in Asia (the Ganges–Brahmaputra, Mekong and Yangtze). Both CYGNSS (SWE_{CYGNSS}) and GIEMS (SWE_{GIEMS}) surface water extent time series are shown for all the basins with the MODIS-based estimates (SWE_{MODIS}) when available.

SWE_{CYGNSS} and SWE_{GIEMS} show a nearly identical seasonality in all the river basins studied, with a correlation above 0.9 in most of the cases. Their estimations at low water stage are close in all study areas except in the Yangtze, which is remarkable as WF_{CYGNSS} is retrieved independantly from GIEMS. Moreover, the seasonal amplitude in WF_{CYGNSS} and WF_{GIEMS} are close in five basins: the Orinoco, Amazon, Parana/La Plata, Lake Chad and Congo. GIEMS shows a higher peak surface water extent in the IND and in the study areas located in Asia, where monsoon regimes produce intense seasonal rainfall.

The comparison of SWE_{CYGNSS} and SWE_{GIEMS} against MODIS-based estimations (SWE_{MODIS}) in the IND and LMB is consistent. SWE_{MODIS} presents a similar seasonality with a quite lower amplitude than SWE_{CYGNSS} (much lower than SWE_{GIEMS}). In these two study areas, both the spatial (Figure S3 and Fig. 10) and temporal variations of surface water extent are correctly captured in our CYGNSS-derived estimations. The larger seasonal flood signal in GIEMS

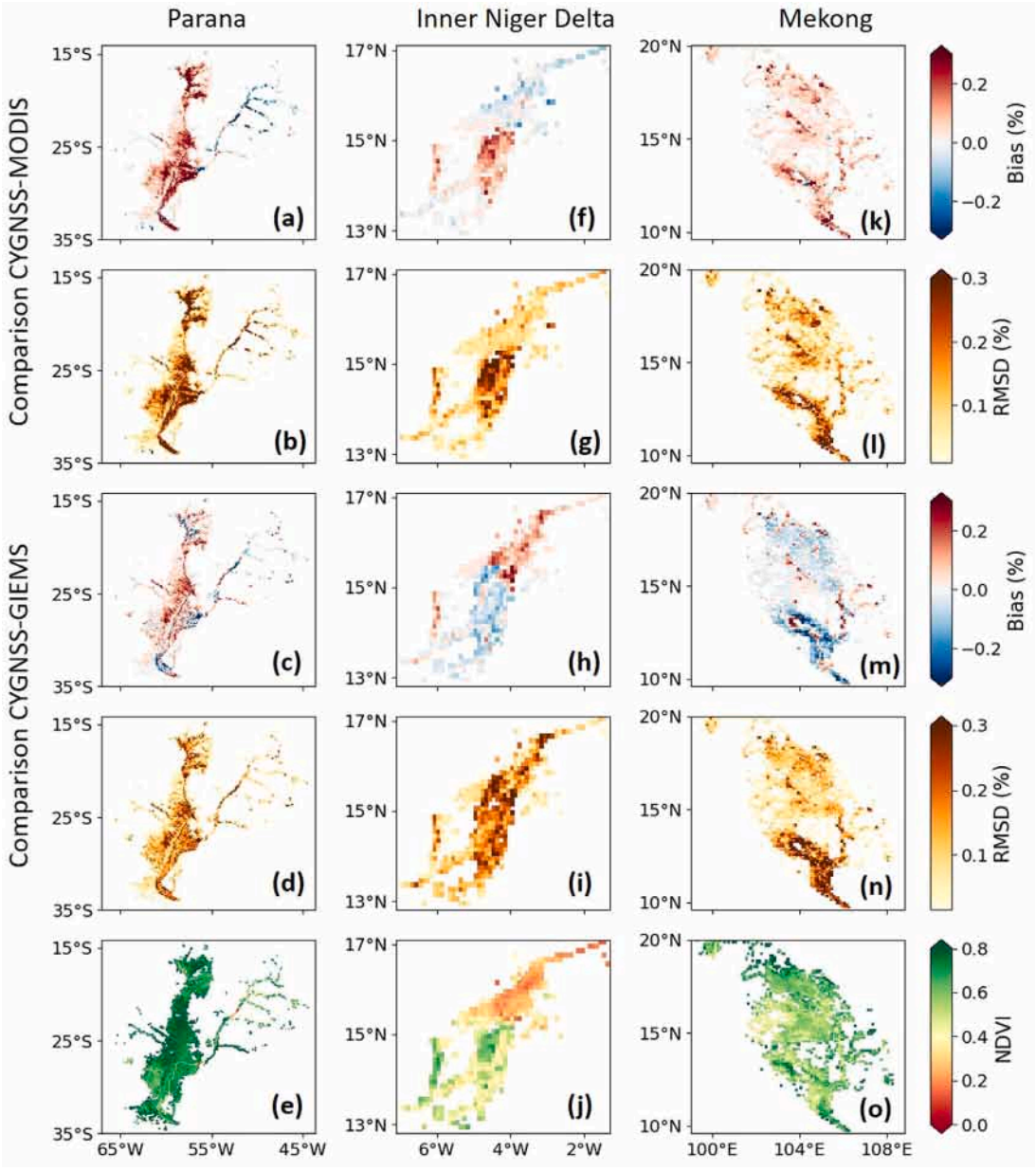

Fig. 10. Pixel-by-pixel bias and RMSD obtained between WF_{CYGNSS} and either WF_{MODIS} (top two rows) or WF_{GIEMS} (3rd and 4th rows). The last row shows MODIS yearly maximum NDVI in each study area. (a–d) Results over the Parana, (e–h) results over the Inner Niger Delta (IND), and (i–l) results over the Lower Mekong. A positive bias (pixels in red in subplots a,c,f,h,k,m) means WF_{CYGNSS} is greater than the other dataset. (For interpretation of the references to color in this figure legend, the reader is referred to the web version of this article.)

when compared to both CYGNSS and MODIS indicates a likely overestimation of surface water extent in the IND and LMB by the former, likely due to a high soil moisture content during the wet season. Conversely, the comparison of SWE_{CYGNSS} and SWE_{GIEMS} in the Parana is very consistent both in seasonality and in amplitude, while SWE_{MODIS} shows a much lower surface water extent at high water stage. As it was previously pointed out, this is likely due to the higher vegetation density found in the Parana during the wet season. This produces abnormally low WF estimates by MODIS at high water stage in areas such as the Pantanal wetlands. It is worth noting that although WF_{CYGNSS} was trained with WF_{MODIS}, it compares as well with GIEMS as with MODIS surface water extent.

Finally, the surface water extent estimations from JERS-1 (SWE_{JERS}) at high and low water stages in the Amazon are indicated in Fig. 11 in dark and light green, respectively. It is in both cases much higher than the corresponding seasonal estimations from SWE_{CYGNSS} and SWE_{GIEMS}. It suggests a possible underestimation of flood extent in the Amazon as the GNSS-R coherent signal can be attenuated or even lost with dense vegetation layers (Loria et al., 2020). The L-band SAR-based wetland maps over the Amazon and the Congo basins indicate a higher surface water extent at high water stage than both SWE_{CYGNSS} and SWE_{GIEMS} (see Fig. 9 and Figure S2, respectively). However, the SAR data used to create these maps are from 1995–1996 and 2009–2010 and a direct comparison thus neglects the interannual variability as well as possible climate trends. Furthermore, an inter-comparison of existing inundation datasets in the Amazon basin was recently performed by Fleischmann et al. (2022). It concludes that the SAR-based datasets (and especially the wetland maps from Hess et al. (2015) we used in this study) systematically give a higher flood extent than other methods. The long-term minimum and maximum surface water extents given by this inter-comparison are 490,300 ± 204,800 km^2 and 139,300 ± 127,800 km^2, respectively. Both SWE_{CYGNSS} and

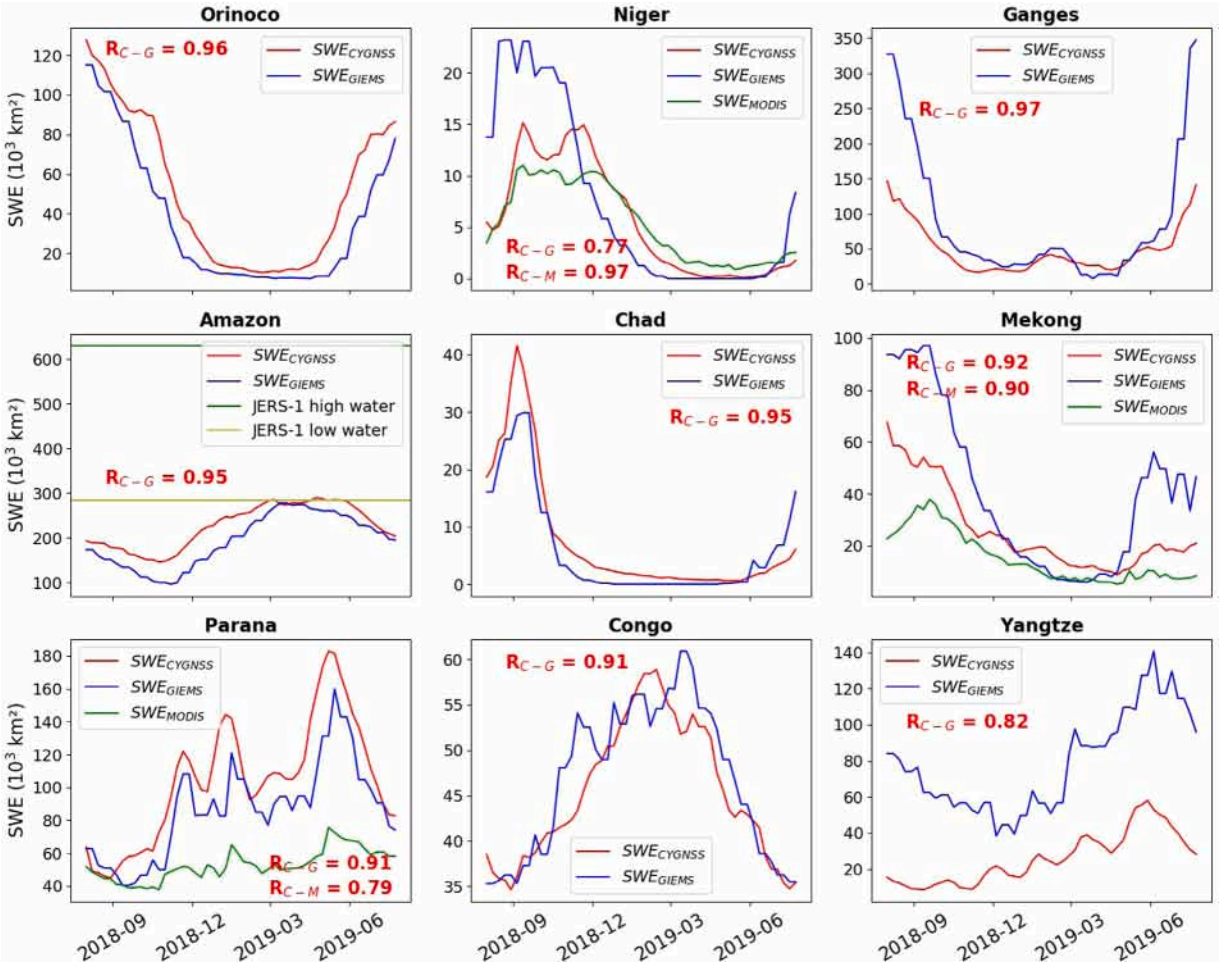

Fig. 11. Time series of weekly surface water extent estimated from CYGNSS and GIEMS (upsampled from the 10-day GIEMS product), averaged for 9 River basins: (a) Orinoco, (b) Amazon, (c) Parana/La Plata, (d) IND, (e) Chad (f), Congo, (g) Ganges-Brahmaputra, (h) LMB, and (i) Yangtze. Also shown, the MODIS surface water extent time series for the Parana, IND and LMB, and the surface water extent at high and low water stages in the Amazon from Hess et al. (2015). The correlations between the time series of SWE_{CYGNSS} and SWE_{GIEMS} (R_{C-G}) and, when exist, SWE_{MODIS} (R_{C-M}), are printed in red in each subplot. (For interpretation of the references to color in this figure legend, the reader is referred to the web version of this article.)

SWE_{GIEMS} at low and high water stages in 2018–2019 are within the range of these results when taking the large uncertainties into account.

4.6. Spatiotemporal dynamics of inundations

To highlight the potential of this new dataset for hydrological studies, we take here the example of the Llanos de Mojos in the South of the Amazon basin. The inundations in these complex and large wetlands are generated by both an endogenous process fed by local precipitation, and an exogenous process due to a flood wave in the Mamore River generated by intense rainfall over the Andes Range (Bourrel et al., 2009). The flooded savannas around the Mamore, Beni, and Itenez rivers correspond well to the spatial extent of inundations derived from both JERS-1 and CYGNSS (Fig. 9). If we consider a square box between −68° and −61° longitude and between −16.5° and −11.5° latitude, centered on the Mamoré River, the maximum surface water extent retrieved with CYGNSS and GIEMS are ~79,300 and ~80,050 km^3, respectively. This is close to the yearly maximum inundation extent observed in this region with the Scanning Multichannel Microwave Radiometer (SMMR) between 1979 and 1987 by Hamilton et al. (2004), for example. The weekly information of WF_{CYGNSS} at 0.1° could be further used to decompose the different flooding processes and their respective spatial extents, as achieved in Bourrel et al. (2009) for the 1997–1998 El-Niño event.

5. Discussion

The methodology developed here was shown to be efficient for mapping the spatiotemporal variations of inundation extent over the tropics. A special attention was given to the performances over vegetated regions including the dense tropical forests of the Amazon and Congo basins. While the results presented above prove that both the spatial distribution and the temporal variations of surface water extent are consistent with most of the regional reference datasets, a large dispersion was also highlighted (RMSD ~20%, R ~0.60). We discuss here the choice of the methodology and some sources of error in our retrieval model. We also highlight the large interest of CYGNSS and spaceborne GNSS-R for monitoring the spatiotemporal dynamics of inundations at large scale.

5.1. Retrieval model

The retrieval model proposed in this study is quite simple as it is based on the assumption of the linearity between Γ_{mean} and the Water Fraction. Previous studies stated, on the contrary, that relationships between CYGNSS reflectivity and the surface water are non-linear (Chew and Small, 2020b). Here, we use the redundancy of CYGNSS observations within each pixel and compute their distribution statistics. The linearity between Γ_{mean} (in linear units) and the Water Fraction was illustrated in Fig. 3 for different AGB values. These curves were

computed using the average Γ_{mean} per Water Fraction bin (2% bins) instead of all samples in the learning dataset. The linear relationships computed this way are more robust to noise, and they were shown to better represent the spatiotemporal variations of inundations. The few pixels affected by a large Water Fraction were underestimated when using all the samples of the learning dataset, dominated by low WF.

We identified the contribution of the vegetation to the GNSS-R signal and developed a correction for this effect. We used the AGB maps from GlobBiomass (Santoro, 2018; Santoro et al., 2021) to bin the learning dataset. Inside a single AGB interval, Γ_{mean} was expected to vary linearly with the Water Fraction (see Fig. 3). On the contrary, the slope and intercept of this linear relationship vary depending on the average AGB in the pixel, as shown in Fig. 4. This was better modeled using a third order polynomial fit, such that the final expression of the relationship between Γ_{mean}, the AGB, and the Water Fraction comprises 8 unknowns (a_i and $b_i, i \in [0,3]$ in Eq. (6)). Modeling the attenuation of GNSS-R signals by the vegetation and its influence on Γ_{mean} was essential to correctly represent the dynamics of floods in densely vegetated regions. It permitted to retrieve fractional inundations in pixels with an average AGB up to ~300 Mg/ha in the Congo and Amazon basins. Our methodology is based on a statistical more than physical approach of the link between CYGNSS reflectivity and the Water Fraction. Still, the evolution of slope and intercept against the AGB may be physically-interpreted. For a moderate AGB, GNSS-R signals over areas with low WF values are rapidly attenuated. On the contrary, a strong forward scattering is still found over large floodplains. This is a possible explanation for the intercept tending toward zero while the slope slightly decreases in the 0–100 Mg/ha AGB range. For high-AGB values, GNSS-R signals are strongly attenuated whatever the flooding state. This explains the late and important slope increase in our model, to account for the large decrease of Γ_{mean} over flooded areas.

Other geophysical parameters are not taken into account in our retrieval model. The surface roughness and SM are commonly used to describe the coherent reflected power, through the Rayleigh parameter and the Fresnel reflection coefficients (De Roo and Ulaby, 1994; Voronovich and Zavorotny, 2018). They also have been used to parameterize the response of CYGNSS reflectivity to the presence of surface water (Chew and Small, 2020b). In the next section, we investigate the sensitivity of CYGNSS Water Fractions compared to the reference datasets for different geophysical parameters, including SM.

5.2. Sources of error

We used the SMAP enhanced L3 9 km SM version 5 product regridded at 0.1° and 7-day spatiotemporal resolution to analyze the influence of the SM content on the results. The biases and the RMSD between WF_{CYGNSS} and WF_{MODIS} (C-M) and between WF_{CYGNSS} and WF_{GIEMS} (C-G) were computed in 1% SM bins, and they are shown in Fig. 12a-c for the Parana, IND and Mekong basins, respectively. For the three basins, a similar pattern can be observed for the comparison between CYGNSS and MODIS. The bias is around 0 for SM $\leq 0.3\,cm^3/cm^3$, and then reaches 10%–20% for SM $> 0.4\,cm^3/cm^3$. This reveals a logical overestimation of the WF derived from CYGNSS for wet soils, as during intense rainfall periods. It is consistent with the coherency of GNSS-R signals over saturated soils which was highlighted in Collett et al. (2022), for example. On the contrary, the comparison between CYGNSS and GIEMS does not show a significant trend on the evolution of the biases across the three study areas. A larger RMSD was found for high SM values, but it could be linked to larger floods during the rainfall events. A negative bias is found over wet soils in the IND and Mekong basins, which is consistent with the results from Fig. 11 suggesting an overestimation of the inundated areas by GIEMS during the large West African and Southeast Asian monsoons. Finally, note that the SM derived from L-band radiometers (SMAP and SMOS) is particularly affected by the presence of surface water, which introduces an overestimation of the SM during the wet season. This limits the use of ancillary information in our retrieval model to correct the sensitivity of GNSS-R observations to SM.

Fig. 12d–f shows a similar analysis conducted on the MODIS NDVI values. Although we took into account the biomass in our retrieval model, the vegetation has strong seasonal variations and can be the cause of an underestimation of flooded areas, especially for the optical sensors. It is also worth noting that the SM and NDVI have similar seasonal variations and can be highly correlated. Here, contrasting behaviors are observed in the three study areas. Over the Parana, the bias between WF_{CYGNSS} and WF_{MODIS} is negative for NDVI < 0.4 and positive otherwise. CYGNSS estimations are greater than MODIS over most of the NDVI range, while Fig. 10 highlighted the high NDVI values at high water stage in the Parana. This backs up the hypothesis of an underestimation of the surface water extent from MODIS due to vegetation growth, while CYGNSS and GIEMS are in good agreement. In the IND, a positive bias between WF_{CYGNSS} and WF_{MODIS} was also observed for NDVI > 0.3. It could explain the larger amplitude observed in CYGNSS and GIEMS in the central part of the IND at high water stage (see Figure S3 and Fig. 10). Over the Mekong, a small positive bias is found over the full NDVI range. Finally, the biases computed between WF_{CYGNSS} and WF_{GIEMS} mostly vary from ±10%, with obvious spatial patterns observed across the three study areas.

Due to the lack of a consistent dataset of soil roughness at the scale of the GPS L1 wavelength, this parameter was not studied. According to models, an underestimation of fractional inundations is expected when the surface roughness is high (Chew and Small, 2020b), because of the loss of coherency in the GNSS-R signals (Loria et al., 2020). We evaluated the influence of the topography (*i.e.* large scale roughness) on the statistical comparisons performed between WF_{CYGNSS}, WF_{MODIS} and WF_{GIEMS} in the Parana and the Mekong basins. For this, we used the SRTM30+ Global 1-km Digital Elevation Model (DEM) Version 11 for land surfaces (Sandwell et al., 2014), distributed by the Pacific Islands Ocean Observing System (PacIOOS). The std height in each 0.1° pixel was computed and was used to bin the compared datasets, and the results are presented in Figure S4. Surprisingly, no significant differences were observed between the samples with high and low large scale roughness. On the same figure, we evaluated the evolution of the statistics depending on the AGB. Logically, consistent results were obtained across the full AGB range in both Parana and Mekong basins, because it was used as input to parameterize our model. Finally, the barplots in Figure S4 present the same statistics computed for each general land cover type, derived from the ESA CCI land cover maps at 300 m resolution (ESA, 2017). The largest RMSD were obtained for the open water and flooded herbaceous classes, in addition to the irrigated croplands in the Mekong basin and especially in the Mekong Delta. The biases of CYGNSS versus MODIS are largely positive for the vegetated classes (irrigated cropland and flooded herbaceous). This is another element indicating that MODIS is likely to underestimate the inundation extent due to the limitations of optical signals over vegetated wetlands.

6. Conclusion

In this study we proposed an algorithm for retrieving weekly fractions of water at 0.1° spatial resolution based on CYGNSS reflectivity. We assumed that the fraction of water in a pixel increases linearly with Γ_{mean}, within each 5 Mg/ha range of biomass. Third order polynomial fits against the AGB were used to account for the influence of the vegetation on GNSS-R signals. The final model comprises 8 parameters that were fitted using a learning dataset. We used reference surface water maps based on MODIS over the Parana, Niger, and Mekong basins and based on JERS-1 over the Amazon basin, for estimating the model parameters required to further compute CYGNSS fractions of water (WF_{CYGNSS}). We also used GIEMS at global scale for an independent comparison with our intertropical estimations of inundation extent.

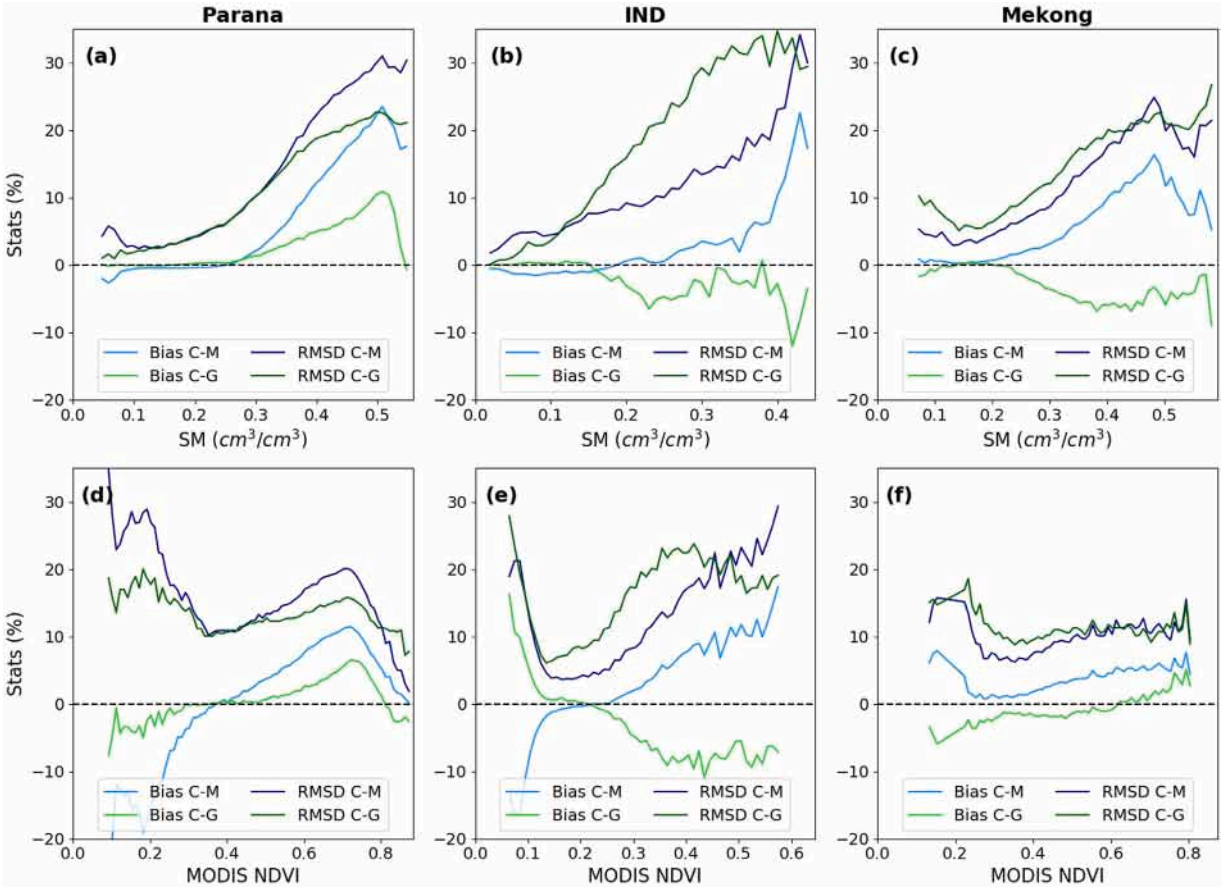

Fig. 12. Influence of the soil moisture (SM) and vegetation (NDVI) on the result of the statistical comparisons conducted between WF_{CYGNSS}, WF_{GIEMS} and WF_{MODIS} over the Parana, IND and Mekong basins. (a–c) Bias and RMSD computed between WF_{CYGNSS} and WF_{MODIS} (C–M) and between WF_{CYGNSS} and WF_{GIEMS} (C–G), as a function of the SM content. (d–f) Same statistics computed as a function of the NDVI from MODIS. The statistics were computed for 1% SM and 0.01 NDVI bins. Only bins with at least 200 samples are shown here for the sake of robustness.

Our retrieval model demonstrated good performances over most selected river basins. The spatial distribution of inundations at high water stage is in good agreement with the reference maps, except over the Parana basin where MODIS may be affected by the vegetation growth, and over the Cuvette Centrale of Congo where long-term inundation signals are detected but not short-term flood pulses under the densest canopies. WF_{CYGNSS} matches well the seasonality of WF_{MODIS} and WF_{GIEMS} datasets and the time series of total inundated areas are consistent with the former, except once again over the Parana basin. Statistically, our estimations were compared at the regional scale with MODIS and GIEMS datasets and we obtained a RMSD of ~20% and a correlation of ~0.60. A positive bias was found between WF_{CYGNSS} and WF_{MODIS}. Two factors were identified to account for these differences: (i) an overestimation of WF_{CYGNSS} over saturated soils, when the SM exceeds 0.3–0.4 cm^3/cm^3, and (ii) an underestimation of WF_{MODIS} at high water stage due to the vegetation growth, when the NDVI exceeds 0.4–0.5 (especially in the Parana basin). On the contrary, the comparisons of WF_{CYGNSS} and WF_{GIEMS} show low biases, despite some deviation in the estimations illustrated by a global RMSD of 15.0%. It is finally worth noting that WF_{MODIS} and WF_{GIEMS} are subjected to their own, large uncertainties.

Overall, we evaluated the WF maps proposed over a large range of environments, spanning from the semi-arid areas in the IND to the dense tropical forests in the Amazon and Congo basins. Some limitations are still to be taken into account in our retrieval model, *e.g.* the overestimation highlighted over saturated soils and coastal pixels. Nevertheless, we also highlighted the large benefit of these estimations over tropical wetlands for the hydrological community. First, WF_{CYGNSS} shows a much higher level of spatial detail than previously obtained with GIEMS, due to the higher spatial resolution of CYGNSS coherent observations and their averaging into a 0.1° grid (against 0.25° for GIEMS). Then, the weekly time sampling allows a fine mapping of the inundation dynamics, for regions affected by short or multiple flood pulses. Finally, CYGNSS has been operating since 2016 and its successors like the ESA's HydroGNSS mission will extend both the current time series of spaceborne GNSS-R acquisitions over the tropics and its spatial coverage, especially over polar regions.

CRediT authorship contribution statement

Pierre Zeiger: Conceptualization, Methodology, Software, Formal analysis, Investigation, Resources, Data curation, Writing – original draft, Writing – review & editing, Visualization. **Frédéric Frappart:** Conceptualization, Validation, Formal analysis, Resources, Supervision, Project administration, Funding acquisition. **José Darrozes:** Conceptualization, Validation, Formal analysis, Resources. **Catherine Prigent:** Validation, Formal analysis, Resources, Data curation. **Carlos Jiménez:** Validation, Data curation. **Luc Bourrel:** Validation, Formal analysis.

Declaration of competing interest

The authors declare the following financial interests/personal relationships which may be considered as potential competing interests: Frederic Frappart reports financial support was provided by French Space Agency. Frederic Frappart reports financial support was provided by National Centre for Scientific Research.

Data availability

The data are referenced in the "Data availability" section.

Acknowledgments

P. Zeiger is funded by a PhD grant from Ministère de l'Enseignement Supérieur, de la Recherche et de l'Innovation (MESRI), France. This work was supported by Centre National de la Recherche Scientifique (CNRS), France and Centre National d'Etudes Spatiales (CNES), France through INSU PNTS grant URGENS and TOSCA grants SWHYM and SCOMAG, respectively. We thank all the reviewers for their helpful and detailed suggestions, to help us improve the revised version of this manuscript.

Appendix A. Supplementary data

Supplementary material related to this article can be found online at https://doi.org/10.1016/j.jhydrol.2023.130305.

References

Acreman, M., Holden, J., 2013. How wetlands affect floods. Wetlands 33 (5), 773–786. http://dx.doi.org/10.1007/s13157-013-0473-2.

Al-Khaldi, M.M., Johnson, J.T., Gleason, S., Chew, C.C., Gerlein-Safdi, C., Shah, R., Zuffada, C., 2021a. Inland water body mapping using CYGNSS coherence detection. IEEE Trans. Geosci. Remote Sens. 59 (9), 7385–7394. http://dx.doi.org/10.1109/TGRS.2020.3047075.

Al-Khaldi, M.M., Johnson, J.T., Gleason, S., Loria, E., O'Brien, A.J., Yi, Y., 2021b. An algorithm for detecting coherence in cyclone global navigation satellite system mission level-1 delay-Doppler maps. IEEE Trans. Geosci. Remote Sens. 59 (5), 4454–4463. http://dx.doi.org/10.1109/TGRS.2020.3009784.

Al-Khaldi, M.M., Johnson, J.T., O'Brien, A.J., Balenzano, A., Mattia, F., 2019. Time-series retrieval of soil moisture using CYGNSS. IEEE Trans. Geosci. Remote Sens. 57 (7), 10.

Bergamaschi, P., Frankenberg, C., Meirink, J.F., Krol, M., Dentener, F., 2007. Satellite chartography of atmospheric methane from SCIAMACHY on board ENVISAT: 2. Evaluation based on inverse model simulations. J. Geophys. Res. 112 (D2), D02304. http://dx.doi.org/10.1029/2006JD007268.

Bergé-Nguyen, M., Crétaux, J.-F., 2015. Inundations in the Inner Niger Delta: Monitoring and analysis using MODIS and global precipitation datasets. Remote Sens. 7 (2), 2127–2151.

Berndt, D.J., Clifford, J., 1994. Using dynamic time warping to find patterns in time series. In: AAAI-94 Workshop on Knowledge Discovery in Databases, Vol. 10. pp. 359–370.

Betbeder, J., Gond, V., Frappart, F., Baghdadi, N.N., Briant, G., Bartholome, E., 2014. Mapping of central africa forested wetlands using remote sensing. IEEE J. Sel. Top. Appl. Earth Obs. Remote Sens. 7 (2), 531–542. http://dx.doi.org/10.1109/JSTARS.2013.2269733.

Bourrel, L., Phillips, L., Moreau, S., 2009. The dynamics of floods in the Bolivian Amazon Basin. Hydrol. Process. 23 (22), 3161–3167.

Bullock, A., Acreman, M., 2003. The role of wetlands in the hydrological cycle. Hydrol. Earth Syst. Sci. 7 (3), 358–389. http://dx.doi.org/10.5194/hess-7-358-2003.

Camps, A., 2019. Spatial resolution in GNSS-R under coherent scattering. IEEE Geosci. Remote Sens. Lett. 17 (1), 32–36.

Camps, A., Park, H., Pablos, M., Foti, G., Gommenginger, C.P., Liu, P.W., Judge, J., 2016. Sensitivity of GNSS-R spaceborne observations to soil moisture and vegetation. IEEE J. Sel. Top. Appl. Earth Obs. Remote Sens. 9 (10), 4730–4742. http://dx.doi.org/10.1109/JSTARS.2016.2588467.

Cardellach, E., Ao, C., De la Torre Juárez, M., Hajj, G., 2004. Carrier phase delay altimetry with GPS-reflection/occultation interferometry from low Earth orbiters. Geophys. Res. Lett. 31 (10).

Carreno-Luengo, H., Luzi, G., Crosetto, M., 2020. Above-ground biomass retrieval over tropical forests: A novel GNSS-R approach with CyGNSS. Remote Sens. 12 (9), 1368.

Chapman, B., McDonald, K., Shimada, M., Rosenqvist, A., Schroeder, R., Hess, L., 2015. Mapping regional inundation with spaceborne L-Band SAR. Remote Sens. 7 (5), 5440–5470. http://dx.doi.org/10.3390/rs70505440.

Chapman, B.D., Russo, I.M., Galdi, C., Morris, M., di Bisceglie, M., Zuffada, C., Downs, B., Lavalle, M., Loria, E., O'Brien, A.J., 2022. Comparison of SAR and CYGNSS surface water extent metrics. IEEE J. Sel. Top. Appl. Earth Obs. Remote Sens. 15, 3235–3245. http://dx.doi.org/10.1109/JSTARS.2022.3162764.

Chew, C., Reager, J.T., Small, E., 2018. CYGNSS data map flood inundation during the 2017 Atlantic hurricane season. Sci. Rep. 8 (1), 9336. http://dx.doi.org/10.1038/s41598-018-27673-x.

Chew, C., Shah, R., Zuffada, C., Hajj, G., Masters, D., Mannucci, A.J., 2016. Demonstrating soil moisture remote sensing with observations from the UK TechDemoSat-1 satellite mission. Geophys. Res. Lett. 43 (7), 3317–3324. http://dx.doi.org/10.1002/2016GL068189.

Chew, C.C., Small, E.E., 2018. Soil moisture sensing using spaceborne GNSS reflections: Comparison of CYGNSS reflectivity to SMAP soil moisture. Geophys. Res. Lett. 45 (9), 4049–4057. http://dx.doi.org/10.1029/2018GL077905.

Chew, C., Small, E., 2020a. Description of the UCAR/CU soil moisture product. Remote Sens. 12 (10), 1558. http://dx.doi.org/10.3390/rs12101558.

Chew, C., Small, E., 2020b. Estimating inundation extent using CYGNSS data: A conceptual modeling study. Remote Sens. Environ. 246, 111869. http://dx.doi.org/10.1016/j.rse.2020.111869.

Chew, C., Small, E., Huelsing, H., 2023. Flooding and inundation maps using interpolated CYGNSS reflectivity observations. Remote Sens. Environ. 293, 113598.

Choudhury, B.J., 1991. Passive microwave remote sensing contribution to hydrological variables. Surv. Geophys. 12, 63–84.

Clarizia, M.P., Pierdicca, N., Costantini, F., Floury, N., 2019. Analysis of CYGNSS data for soil moisture retrieval. IEEE J. Sel. Top. Appl. Earth Obs. Remote Sens. 12 (7), 9.

Clarizia, M.P., Ruf, C.S., 2016. Wind speed retrieval algorithm for the cyclone global navigation satellite system (CYGNSS) mission. IEEE Trans. Geosci. Remote Sens. 54 (8), 4419–4432. http://dx.doi.org/10.1109/TGRS.2016.2541343.

Clarizia, M.P., Ruf, C.S., Cipollini, P., Zuffada, C., 2016. First spaceborne observation of sea surface height using GPS-Reflectometry. Geophys. Res. Lett. 43 (2), 767–774. http://dx.doi.org/10.1002/2015GL066624.

Collett, I., Wang, Y., Shah, R., Morton, Y.J., 2022. Phase coherence of GPS signal land reflections and its dependence on surface characteristics. IEEE Geosci. Remote Sens. Lett. 19, 1–5. http://dx.doi.org/10.1109/LGRS.2021.3094407.

CYGNSS, 2020. CYGNSS Level 1 Science Data Record Version 3.0. Ver. 3.0. PO.DAAC, CA, USA, URL: https://doi.org/10.5067/CYGNS-L1X30. accessed: 2021-10-01.

Davidson, N.C., Fluet-Chouinard, E., Finlayson, C.M., 2018. Global extent and distribution of wetlands: trends and issues. Mar. Freshwater Res. 69 (4), 620. http://dx.doi.org/10.1071/MF17019.

De Roo, R.D., Ulaby, F.T., 1994. Bistatic specular scattering from rough dielectric surfaces. IEEE Trans. Antennas and Propagation 42 (2), 220–231.

Dubayah, R., Armston, J., Healey, S.P., Bruening, J.M., Patterson, P.L., Kellner, J.R., Duncanson, L., Saarela, S., Ståhl, G., Yang, Z., Tang, H., Blair, J.B., Fatoyinbo, L., Goetz, S., Hancock, S., Hansen, M., Hofton, M., Hurtt, G., Luthcke, S., 2022. GEDI launches a new era of biomass inference from space. Environ. Res. Lett. 17 (9), 095001. http://dx.doi.org/10.1088/1748-9326/ac8694.

Eroglu, O., Kurum, M., Boyd, D., Gurbuz, A.C., 2019. High spatio-temporal resolution cygnss soil moisture estimates using artificial neural networks. Remote Sens. 11 (19), http://dx.doi.org/10.3390/rs11192272.

ESA, 2017. Land Cover CCI Product User Guide Version 2. Tech. Rep. (2017), URL: maps.elie.ucl.ac.be/CCI/viewer/download/ESACCI-LC-Ph2-PUGv2_2.0.pdf.

Feng, M., Sexton, J.O., Channan, S., Townshend, J.R., 2016. A global, high-resolution (30-m) inland water body dataset for 2000: First results of a topographic–spectral classification algorithm. Int. J. Digit. Earth 9 (2), 113–133. http://dx.doi.org/10.1080/17538947.2015.1026420.

Fleischmann, A.S., Papa, F., Fassoni-Andrade, A., Melack, J.M., Wongchuig, S., Paiva, R.C.D., Hamilton, S.K., Fluet-Chouinard, E., Barbedo, R., Aires, F., et al., 2022. How much inundation occurs in the Amazon River basin? Remote Sens. Environ. 278, 113099.

Foti, G., Gommenginger, C., Jales, P., Unwin, M., Shaw, A., Robertson, C., Roselló, J., 2015. Spaceborne GNSS reflectometry for ocean winds: First results from the UK TechDemoSat-1 mission. Geophys. Res. Lett. 42 (13), 5435–5441. http://dx.doi.org/10.1002/2015GL064204.

Frappart, F., Biancamaria, S., Normandin, C., Blarel, F., Bourrel, L., Aumont, M., Azemar, P., Vu, P.-L., Le Toan, T., Lubac, B., Darrozes, J., 2018. Influence of recent climatic events on the surface water storage of the Tonle Sap Lake. Sci. Total Environ. 636, 1520–1533. http://dx.doi.org/10.1016/j.scitotenv.2018.04.326.

Gerlein-Safdi, C., Bloom, A.A., Plant, G., Kort, E.A., Ruf, C.S., 2021. Improving representation of tropical wetland methane emissions with CYGNSS inundation maps. Glob. Biogeochem. Cycles 35 (12), e2020GB006890. http://dx.doi.org/10.1029/2020GB006890.

Gerlein-Safdi, C., Ruf, C.S., 2019. A CYGNSS-based algorithm for the detection of inland waterbodies. Geophys. Res. Lett. 46 (21), 12065–12072. http://dx.doi.org/10.1029/2019GL085134.

Ghasemigoudarzi, P., Huang, W., De Silva, O., Yan, Q., Power, D.T., 2020. Flash flood detection from CYGNSS data using the RUSBoost algorithm. IEEE Access 8, 171864–171881. http://dx.doi.org/10.1109/ACCESS.2020.3025302.

Gleason, S., O'Brien, A., Russel, A., Al-Khaldi, M.M., Johnson, J.T., 2020. Geolocation, calibration and surface resolution of CYGNSS GNSS-R land observations. Remote Sens. 12 (8), http://dx.doi.org/10.3390/rs12081317.

Hamilton, S.E., Casey, D., 2016. Creation of a high spatio-temporal resolution global database of continuous mangrove forest cover for the 21st century (CGMFC-21). Global Ecol. Biogeogr. 25 (6), 729–738.

Hamilton, S.K., Sippel, S.J., Melack, J.M., 2004. Seasonal inundation patterns in two large savanna floodplains of South America: the Llanos de Moxos(Bolivia) and the Llanos del Orinoco(Venezuela and Colombia). Hydrol. Process. 18 (11), 2103–2116. http://dx.doi.org/10.1002/hyp.5559.

Hess, L.L., Melack, J.M., Affonso, A.G., Barbosa, C., Gastil-Buhl, M., Novo, E.M., 2015. Wetlands of the lowland Amazon basin: Extent, vegetative cover, and dual-season inundated area as mapped with JERS-1 synthetic aperture radar. Wetlands 35 (4), 745–756. http://dx.doi.org/10.1007/s13157-015-0666-y.

Hess, L., Melack, J., Filoso, S., Wang, Y., 1995. Delineation of inundated area and vegetation along the Amazon floodplain with the SIR-C synthetic aperture radar. IEEE Trans. Geosci. Remote Sens. 33 (4), 896–904. http://dx.doi.org/10.1109/36.406675.

Hess, L.L., Melack, J.M., Novo, E.M., Barbosa, C.C., Gastil, M., 2003. Dual-season mapping of wetland inundation and vegetation for the central Amazon basin. Remote Sens. Environ. 87 (4), 404–428. http://dx.doi.org/10.1016/j.rse.2003.04.001.

Huete, A., Liu, H., Batchily, K., van Leeuwen, W., 1997. A comparison of vegetation indices over a global set of TM images for EOS-MODIS. Remote Sens. Environ. 59 (3), 440–451. http://dx.doi.org/10.1016/S0034-4257(96)00112-5.

Jensen, K., Mcdonald, K., 2019. Surface water microwave product series Version 3: a near-real time and 25-year historical global inundated area fraction time series from active and passive microwave remote sensing. IEEE Geosci. Remote Sens. Lett. 16 (9), 1402–1406. http://dx.doi.org/10.1109/LGRS.2019.2898779.

Jensen, K., McDonald, K., Podest, E., Rodriguez-Alvarez, N., Horna, V., Steiner, N., 2018. Assessing L-Band GNSS-reflectometry and imaging radar for detecting sub-canopy inundation dynamics in a tropicalwetlands complex. Remote Sens. 10 (9), http://dx.doi.org/10.3390/rs10091431.

Junk, W.J., An, S., Finlayson, C., Gopal, B., Květ, J., Mitchell, S.A., Mitsch, W.J., Robarts, R.D., 2013. Current state of knowledge regarding the world's wetlands and their future under global climate change: a synthesis. Aquat. Sci. 75 (1), 151–167.

Kellogg, K.H., Hoffman, P., Standley, S., Shaffer, S.J., Rosen, P.A., Edelstein, W.N., Dunn, C., Baker, C.J., Barela, P.R., Shen, Y., Guerrero, A.M., Xaypraseuth, P., Sagi, V.R., Sreekantha, C.V., Harinath, N., Kumar, R., Bhan, R., Sarma, C., 2020. NASA-ISRO synthetic aperture radar (NISAR) mission. In: 2020 IEEE Aerospace Conference. pp. 1–21.

Li, W., Cardellach, E., Fabra, F., Rius, A., Ribó, S., Martín-Neira, M., 2017. First spaceborne phase altimetry over sea ice using TechDemoSat-1 GNSS-R signals. Geophys. Res. Lett. 44 (16), 8369–8376. http://dx.doi.org/10.1002/2017GL074513.

Li, W., Cardellach, E., Ribó, S., Oliveras, S., Rius, A., 2022. Exploration of multi-mission spaceborne GNSS-R raw IF data sets: Processing, data products and potential applications. Remote Sens. 14 (6), http://dx.doi.org/10.3390/rs14061344.

Li, W., Cardellach, E., Ribó, S., Rius, A., Zhou, B., 2021. First spaceborne demonstration of BeiDou-3 signals for GNSS reflectometry from CYGNSS constellation. Chin. J. Aeronaut. 34 (9), 1–10. http://dx.doi.org/10.1016/j.cja.2020.11.016.

Loria, E., O'Brien, A., Zavorotny, V., Downs, B., Zuffada, C., 2020. Analysis of scattering characteristics from inland bodies of water observed by CYGNSS. Remote Sens. Environ. 245, 111825. http://dx.doi.org/10.1016/j.rse.2020.111825.

Martin-Neira, M., et al., 1993. A passive reflectometry and interferometry system (PARIS): Application to ocean altimetry. ESA J. 17 (4), 331–355.

Martinis, S., Groth, S., Wieland, M., Knopp, L., Rättich, M., 2022. Towards a global seasonal and permanent reference water product from Sentinel-1/2 data for improved flood mapping. Remote Sens. Environ. 278, 113077. http://dx.doi.org/10.1016/j.rse.2022.113077.

Martinis, S., Kersten, J., Twele, A., 2015. A fully automated TerraSAR-X based flood service. ISPRS J. Photogramm. Remote Sens. 104, 203–212. http://dx.doi.org/10.1016/j.isprsjprs.2014.07.014.

Melton, J., Wania, R., Hodson, E., Poulter, B., Ringeval, B., Spahni, R., Bohn, T., Avis, C., Beerling, D., Chen, G., et al., 2013. Present state of global wetland extent and wetland methane modelling: conclusions from a model inter-comparison project (WETCHIMP). Biogeosciences 10 (2), 753–788.

Mitsch, W.J., Bernal, B., Nahlik, A.M., Mander, U., Zhang, L., Anderson, C.J., Jørgensen, S.E., Brix, H., 2013. Wetlands, carbon, and climate change. Landsc. Ecol. 28 (4), 583–597. http://dx.doi.org/10.1007/s10980-012-9758-8.

Morris, M., Chew, C., Reager, J.T., Shah, R., Zuffada, C., 2019. A novel approach to monitoring wetland dynamics using CYGNSS: Everglades case study. Remote Sens. Environ. 233, 111417. http://dx.doi.org/10.1016/j.rse.2019.111417.

Normandin, C., Frappart, F., Lubac, B., Bélanger, S., Marieu, V., Blarel, F., Robinet, A., Guiastrennec-Faugas, L., 2018. Quantification of surface water volume changes in the Mackenzie Delta using satellite multi-mission data. Hydrol. Earth Syst. Sci. 22 (2), 1543–1561. http://dx.doi.org/10.5194/hess-22-1543-2018.

O'Neill, P.E., Chan, S.K., Njoku, E.G., Jackson, T., Bindlish, R., Chaubell, J., Colliander, A., 2021. SMAP Enhanced L3 Radiometer Global and Polar Grid Daily 9 km EASE-Grid Soil Moisture, Version 5. NASA National Snow and Ice Data Center Distributed Active Archive Center, http://dx.doi.org/10.5067/4DQ54OUIJ9DL.

Parrens, M., Al Bitar, A., Frappart, F., Papa, F., Calmant, S., Crétaux, J.-F., Wigneron, J.-P., Kerr, Y., 2017. Mapping dynamic water fraction under the tropical rain forests of the amazonian basin from SMOS brightness temperatures. Water 9 (5), 350. http://dx.doi.org/10.3390/w9050350.

Pekel, J.-F., Cottam, A., Gorelick, N., Belward, A.S., 2016. High-resolution mapping of global surface water and its long-term changes. Nature 540 (7633), 418–422. http://dx.doi.org/10.1038/nature20584.

Pham-Duc, B., Prigent, C., Aires, F., Papa, F., 2017. Comparisons of global terrestrial surface water datasets over 15 years. J. Hydrometeorol. 18 (4), 993–1007. http://dx.doi.org/10.1175/JHM-D-16-0206.1.

Pham-Duc, B., Sylvestre, F., Papa, F., Frappart, F., Bouchez, C., Crétaux, J.-F., 2020. The Lake Chad hydrology under current climate change. Sci. Rep. 10 (1), 1–10. http://dx.doi.org/10.1038/s41598-020-62417-w.

Pierdicca, N., Comite, D., Camps, A., Carreno-Luengo, H., Cenci, L., Clarizia, M.P., Costantini, F., Dente, L., Guerriero, L., Mollfulleda, A., et al., 2021. The potential of spaceborne GNSS reflectometry for soil moisture, biomass, and freeze–thaw monitoring: Summary of a European space agency-funded study. IEEE Geosci. Remote Sens. Mag. 10 (2), 8–38.

Pierdicca, N., Pulvirenti, L., Chini, M., Guerriero, L., Candela, L., 2013. Observing floods from space: Experience gained from COSMO-SkyMed observations. Acta Astronaut. 84, 122–133. http://dx.doi.org/10.1016/j.actaastro.2012.10.034.

Poulter, B., Bousquet, P., Canadell, J.G., Ciais, P., Peregon, A., Saunois, M., Arora, V.K., Beerling, D.J., Brovkin, V., Jones, C.D., et al., 2017. Global wetland contribution to 2000–2012 atmospheric methane growth rate dynamics. Environ. Res. Lett. 12 (9), 094013.

Prigent, C., Jimenez, C., Bousquet, P., 2020. Satellite-derived global surface water extent and dynamics over the last 25 years (GIEMS-2). J. Geophys. Res.: Atmos. 125 (3), http://dx.doi.org/10.1029/2019JD030711.

Prigent, C., Matthews, E., Aires, F., Rossow, W.B., 2001. Remote sensing of global wetland dynamics with multiple satellite data sets. Geophys. Res. Lett. 28 (24), 4631–4634. http://dx.doi.org/10.1029/2001GL013263.

Prigent, C., Papa, F., Aires, F., Rossow, W.B., Matthews, E., 2007. Global inundation dynamics inferred from multiple satellite observations, 1993–2000. J. Geophys. Res. 112 (D12), D12107. http://dx.doi.org/10.1029/2006JD007847.

Pulvirenti, L., Chini, M., Pierdicca, N., Guerriero, L., Ferrazzoli, P., 2011. Flood monitoring using multi-temporal COSMO-SkyMed data: Image segmentation and signature interpretation. Remote Sens. Environ. 115 (4), 990–1002. http://dx.doi.org/10.1016/j.rse.2010.12.002.

Rajabi, M., Nahavandchi, H., Hoseini, M., 2020. Evaluation of CYGNSS observations for flood detection and mapping during sistan and baluchestan torrential rain in 2020. Water 12 (7), 2047. http://dx.doi.org/10.3390/w12072047.

Richards, J.A., Woodgate, P.W., Skidmore, A.K., 1987. An explanation of enhanced radar backscattering from flooded forests. Int. J. Remote Sens. 8 (7), 1093–1100. http://dx.doi.org/10.1080/01431168708954756.

Rodriguez-Alvarez, N., Podest, E., Jensen, K., McDonald, K.C., 2019. Classifying inundation in a tropical wetlands complex with GNSS-R. Remote Sens. 11 (9), 1053. http://dx.doi.org/10.3390/rs11091053.

Rosenqvist, J., Rosenqvist, A., Jensen, K., McDonald, K., 2020. Mapping of maximum and minimum inundation extents in the amazon basin 2014–2017 with ALOS-2 PALSAR-2 ScanSAR time-series data. Remote Sens. 12 (8), http://dx.doi.org/10.3390/rs12081326.

Ruf, C.S., Atlas, R., Chang, P.S., Clarizia, M.P., Garrison, J.L., Gleason, S., Katzberg, S.J., Jelenak, Z., Johnson, J.T., Majumdar, S.J., O'Brien, A., Posselt, D.J., Ridley, A.J., Rose, R.J., Zavorotny, V.U., 2016. New ocean winds satellite mission to probe hurricanes and tropical convection. Bull. Am. Meteorol. Soc. 97 (3), 385–395. http://dx.doi.org/10.1175/BAMS-D-14-00218.1.

Russo, I.M., Bisceglie, M.d., Galdi, C., Lavalle, M., Zuffada, C., 2022. Entropy-based coherence metric for land applications of GNSS-R. IEEE Trans. Geosci. Remote Sens. 60, 1–13. http://dx.doi.org/10.1109/TGRS.2021.3125858.

Sakamoto, T., Van Nguyen, N., Kotera, A., Ohno, H., Ishitsuka, N., Yokozawa, M., 2007. Detecting temporal changes in the extent of annual flooding within the Cambodia and the Vietnamese Mekong Delta from MODIS time-series imagery. Remote Sens. Environ. 109 (3), 295–313. http://dx.doi.org/10.1016/j.rse.2007.01.011.

Sandwell, D., Smith, W., Becker, J., 2014. SRTM30+ global 1-km digital elevation model (DEM): Version 11: Land surface, distributed by the Pacific Islands Ocean Observing System (PacIOOS). URL: http://pacioos.org/metadata/srtm30plus_v11_land.html. Accessed: 2021-11-18.

Santoro, M., 2018. GlobBiomass - global datasets of forest biomass. http://dx.doi.org/10.1594/PANGAEA.894711.

Santoro, M., Cartus, O., Carvalhais, N., Rozendaal, D.M.A., Avitabile, V., Araza, A., de Bruin, S., Herold, M., Quegan, S., Rodríguez-Veiga, P., Balzter, H., Carreiras, J., Schepaschenko, D., Korets, M., Shimada, M., Itoh, T., Moreno Martínez, Á., Cavlovic, J., Cazzolla Gatti, R., da Conceição Bispo, P., Dewnath, N., Labrière, N., Liang, J., Lindsell, J., Mitchard, E.T.A., Morel, A., Pacheco Pascagaza, A.M., Ryan, C.M., Slik, F., Vaglio Laurin, G., Verbeeck, H., Wijaya, A., Willcock, S., 2021. The global forest above-ground biomass pool for 2010 estimated from high-resolution satellite observations. Earth Syst. Sci. Data 13 (8), 3927–3950. http://dx.doi.org/10.5194/essd-13-3927-2021.

Saunois, M., Stavert, A.R., Poulter, B., Bousquet, P., Canadell, J.G., Jackson, R.B., Raymond, P.A., Dlugokencky, E.J., Houweling, S., Patra, P.K., Ciais, P., Arora, V.K., Bastviken, D., Bergamaschi, P., Blake, D.R., Brailsford, G., Bruhwiler, L., Carlson, K.M., Carrol, M., Castaldi, S., Chandra, N., Crevoisier, C., Crill, P.M., Covey, K., Curry, C.L., Etiope, G., Frankenberg, C., Gedney, N., Hegglin, M.I., Höglund-Isaksson, L., Hugelius, G., Ishizawa, M., Ito, A., Janssens-Maenhout, G., Jensen, K.M., Joos, F., Kleinen, T., Krummel, P.B., Langenfelds, R.L., Laruelle, G.G., Liu, L., Machida, T., Maksyutov, S., McDonald, K.C., McNorton, J., Miller, P.A., Melton, J.R., Morino, I., Müller, J., Murguia-Flores, F., Naik, V., Niwa, Y., Noce, S., O'Doherty, S., Parker, R.J., Peng, C., Peng, S., Peters, G.P., Prigent, C., Prinn, R., Ramonet, M., Regnier, P., Riley, W.J., Rosentreter, J.A., Segers, A., Simpson, I.J., Shi, H., Smith, S.J., Steele, L.P., Thornton, B.F., Tian, H., Tohjima, Y., Tubiello, F.N.,

Tsuruta, A., Viovy, N., Voulgarakis, A., Weber, T.S., van Weele, M., van der Werf, G.R., Weiss, R.F., Worthy, D., Wunch, D., Yin, Y., Yoshida, Y., Zhang, W., Zhang, Z., Zhao, Y., Zheng, B., Zhu, Q., Zhu, Q., Zhuang, Q., 2020. The global methane budget 2000–2017. Earth Syst. Sci. Data 12 (3), 1561–1623. http://dx.doi.org/10.5194/essd-12-1561-2020.

Schroeder, R., McDonald, K., Chapman, B., Jensen, K., Podest, E., Tessler, Z., Bohn, T., Zimmermann, R., 2015. Development and evaluation of a multi-year fractional surface water data set derived from active/passive microwave remote sensing data. Remote Sens. 7 (12), 16688–16732. http://dx.doi.org/10.3390/rs71215843.

Scipal, K., Arcioni, M., Chave, J., Dall, J., Fois, F., LeToan, T., Lin, C.-C., Papathanassiou, K., Quegan, S., Rocca, F., Saatchi, S., Shugart, H., Ulander, L., Williams, M., 2010. The BIOMASS mission — An ESA Earth Explorer candidate to measure the BIOMASS of the earth's forests. In: 2010 IEEE International Geoscience and Remote Sensing Symposium. pp. 52–55. http://dx.doi.org/10.1109/IGARSS.2010.5648979.

Sippel, S.J., Hamilton, S.K., Melack, J.M., Choudhury, B.J., 1994. Determination of inundation area in the Amazon River floodplain using the SMMR 37 GHz polarization difference. Remote Sens. Environ. 48 (1), 70–76. http://dx.doi.org/10.1016/0034-4257(94)90115-5.

Tootchi, A., Jost, A., Ducharne, A., 2019. Multi-source global wetland maps combining surface water imagery and groundwater constraints. Earth Syst. Sci. Data 11, 189–220.

Twele, A., Cao, W., Plank, S., Martinis, S., 2016. Sentinel-1-based flood mapping: a fully automated processing chain. Int. J. Remote Sens. 37 (13), 2990–3004. http://dx.doi.org/10.1080/01431161.2016.1192304.

Unwin, M.J., Pierdicca, N., Cardellach, E., Rautiainen, K., Foti, G., Blunt, P., Guerriero, L., Santi, E., Tossaint, M., 2021. An introduction to the HydroGNSS GNSS reflectometry remote sensing mission. IEEE J. Sel. Top. Appl. Earth Obs. Remote Sens. 14, 6987–6999. http://dx.doi.org/10.1109/JSTARS.2021.3089550.

Verpoorter, C., Kutser, T., Seekell, D.A., Tranvik, L.J., 2014. A global inventory of lakes based on high-resolution satellite imagery. Geophys. Res. Lett. 41 (18), 6396–6402. http://dx.doi.org/10.1002/2014GL060641.

Voronovich, A.G., Zavorotny, V.U., 2018. Bistatic radar equation for signals of opportunity revisited. IEEE Trans. Geosci. Remote Sens. 56 (4), 1959–1968. http://dx.doi.org/10.1109/TGRS.2017.2771253.

Wan, W., Liu, B., Zeng, Z., Chen, X., Wu, G., Xu, L., Chen, X., Hong, Y., 2019. Using CYGNSS data to monitor China's flood inundation during typhoon and extreme precipitation events in 2017. Remote Sens. 11 (7), 854. http://dx.doi.org/10.3390/rs11070854.

Wang, J., Hu, Y., Li, Z., 2022. A new coherence detection method for mapping inland water bodies using CYGNSS data. Remote Sens. 14 (13), 3195.

Westerhoff, R., Kleuskens, M., Winsemius, H., Huizinga, H., Brakenridge, G., Bishop, C., 2013. Automated global water mapping based on wide-swath orbital synthetic-aperture radar. Hydrol. Earth Syst. Sci. 17 (2), 651–663.

Whalen, S., 2005. Biogeochemistry of methane exchange between natural wetlands and the atmosphere. Environ. Eng. Sci. 22 (1), 73–94. http://dx.doi.org/10.1089/ees.2005.22.73.

Xiao, X., Boles, S., Liu, J., Zhuang, D., Frolking, S., Li, C., Salas, W., Moore, B., 2005. Mapping paddy rice agriculture in southern China using multi-temporal MODIS images. Remote Sens. Environ. 95 (4), 480–492. http://dx.doi.org/10.1016/j.rse.2004.12.009.

Yamazaki, D., Trigg, M.A., Ikeshima, D., 2015. Development of a global˜ 90 m water body map using multi-temporal Landsat images. Remote Sens. Environ. 171, 337–351. http://dx.doi.org/10.1016/j.rse.2015.10.014.

Yan, Q., Huang, W., Jin, S., Jia, Y., 2020. Pan-tropical soil moisture mapping based on a three-layer model from CYGNSS GNSS-R data. Remote Sens. Environ. 247, 111944. http://dx.doi.org/10.1016/j.rse.2020.111944.

Zavorotny, V.U., Gleason, S., Cardellach, E., Camps, A., 2014. Tutorial on remote sensing using GNSS bistatic radar of opportunity. IEEE Geosci. Remote Sens. Mag. 2 (4), 8–45. http://dx.doi.org/10.1109/MGRS.2014.2374220, Publisher: IEEE.

Zavorotny, V.U., Voronovich, A.G., 2000. Scattering of GPS signals from the ocean with wind remote sensing application. IEEE Trans. Geosci. Remote Sens. 38 (2), 951–964.

Zeiger, P., Frappart, F., Darrozes, J., Prigent, C., Jiménez, C., 2022. Analysis of CYGNSS coherent reflectivity over land for the characterization of pan-tropical inundation dynamics. Remote Sens. Environ. 282, 113278. http://dx.doi.org/10.1016/j.rse.2022.113278.